Antibody-peptide conjugates deliver covalent inhibitors blocking oncogenic cathepsins

Petruzzella, A.; Bruand, M.; Santamaria-Martinez, A.; Katanayeva, N.; Reymond, L.; Wehrle, S.; ... ; Oricchio, E.

nature chemical biology

Article

https://doi.org/10.1038/s41589-024-01627-z

Antibody–peptide conjugates deliver covalent inhibitors blocking oncogenic cathepsins

Received: 10 July 2023

Accepted: 18 April 2024

Published online: 29 May 2024

Check for updates

Aaron Petruzzella[1,2], Marine Bruand[1,2], Albert Santamaria-Martínez[1,2], Natalya Katanayeva[1,2], Luc Reymond[3], Sarah Wehrle[4], Sandrine Georgeon[4], Damla Inel[5,6], Floris J. van Dalen[7,8], David Viertl[9,10], Kelvin Lau[11], Florence Pojer[11], Margret Schottelius[9,12], Vincent Zoete[2,5,6], Martijn Verdoes[7,8], Caroline Arber[5,6], Bruno E. Correia[4] ✉ & Elisa Oricchio[1,2] ✉

Cysteine cathepsins are a family of proteases that are relevant therapeutic targets for the treatment of different cancers and other diseases. However, no clinically approved drugs for these proteins exist, as their systemic inhibition can induce deleterious side effects. To address this problem, we developed a modular antibody-based platform for targeted drug delivery by conjugating non-natural peptide inhibitors (NNPIs) to antibodies. NNPIs were functionalized with reactive warheads for covalent inhibition, optimized with deep saturation mutagenesis and conjugated to antibodies to enable cell-type-specific delivery. Our antibody–peptide inhibitor conjugates specifically blocked the activity of cathepsins in different cancer cells, as well as osteoclasts, and showed therapeutic efficacy in vitro and in vivo. Overall, our approach allows for the rapid design of selective cathepsin inhibitors and can be generalized to inhibit a broad class of proteases in cancer and other diseases.

Several important protein classes, including proteases, kinases, and chaperones are ubiquitously expressed in our body, regulating many physiological processes. However, their activity is frequently co-opted by tumor cells to support malignant growth. Treatment with specific inhibitors blocking the activity of these proteins has the potential to effectively impair tumor growth. Nevertheless, their application in the clinic is limited because of their on-target but off-tumor activity. This poses an important challenge for the development of the next generation of drugs that specifically block the activity of these proteins in tumor cells while sparing normal cells to limit toxicity.

Cysteine cathepsins are a family of 11 proteases regulating several physiological processes[1–4]; these proteases have been considered promising therapeutic targets for the treatment of cancer and other diseases, such as autoimmune disorders and osteoporosis[2,5–7]. Cathepsins are usually synthesized as zymogens and then transported to the lysosome, where the low pH triggers their catalytic activation. In the lysosome, they contribute to protein catabolism[1,8], whereas upon release outside the cell they can participate to the remodeling of the extracellular matrix[3,9]. In tumors, increased cathepsin activity due to mutations or gene overexpression contributes to changes in antigen presentation and interactions with the tumor microenvironment favoring tumor progression and metastasis[2,10–14]. Genetic knockout (KO) of specific cathepsins in transgenic animal models showed that different tumor types depend on the activity of different cathepsins[2,10,15,16]. For example, cathepsin S (CTSS) is predominantly expressed in antigen-presenting cells such as B cells, macrophages and dendritic cells[17,18]. Inhibition of CTSS activity in malignant B cells altered antigen processing and maturation of the major histocompatibility complex class II (MHC-II), inducing an antitumoral immune response and reducing tumor growth[10,11]. Cathepsins B and L (CTSB and CTSL)

A full list of affiliations appears at the end of the paper. ✉e-mail: bruno.correia@epfl.ch; elisa.oricchio@epfl.ch

are ubiquitously expressed in normal tissues[3] but increased activity has been reported in several solid tumors, associated with tumor progression and poor prognosis[16,19–24]. Cathepsin K (CTSK) regulates bone remodeling and favors bone metastasis formation[7,25,26]. Overall, cathepsin activity promotes tumor development by favoring immune evasion, extracellular matrix remodeling or tumor cell migration, indicating that targeting specific cathepsins is necessary in an individual tumor context.

Structural and biochemical characterization[27,28] has been used to profile the substrate selectivity of each protease, which can aid in the design of specific inhibitors. Small molecules inhibiting individual cathepsins have been developed and tested in preclinical and clinical trials[29–39]. However, despite the high in vitro specificity of some of these inhibitors, clinical trials were interrupted because of side effects and/or a lack of efficacy[5,40–42]. These results suggested that these inhibitors either affected the physiological role of these proteins in healthy tissues or were not able to reach the target cells[43]. As an alternative to small-molecule inhibitors, it is possible to use therapeutic peptides to block the proteolytic activity of cathepsins[44,45]. However, their poor pharmacokinetic properties, such as low bioavailability and rapid degradation, limit their application in vivo. Hence, new therapeutic strategies are needed to selectively block the activity of cathepsins in cancer cells while limiting deleterious side effects.

Systemic toxicity is a common problem of routinely adopted chemotherapies designed to induce cytotoxic effects in rapidly proliferating cancer cells. To limit the side effects associated with chemotherapy treatments, cytotoxic drugs have been conjugated with antibodies to guide their delivery and promote selective activity in the tumor cells[46,47]. Antibody–drug conjugates enter the cells by endocytosis and are transported to and confined in the lysosome, where they are degraded[48,49]. The cytotoxic payload is then released from the antibodies, exits the lysosome and reaches the cytosolic compartment where it will be effective. In addition to the classical antibody–drug conjugate combinations where the antibody delivers cytotoxic compounds, it is possible to conjugate antibodies with drugs targeting specific proteins. Hence, we sought to create a modular drug platform to couple non-natural peptide inhibitors (NNPIs) blocking the activity of cysteine cathepsins with antibodies to guide their delivery to the desired type of target cells, thereby creating antibody–peptide inhibitor conjugates (APICs) (Fig. 1a). Importantly, with this approach, we exploited the natural trafficking and accumulation of antibodies in the lysosomes to deliver NNPIs to the compartment where cysteine cathepsins are active (Fig. 1a). Using this antibody-based platform, we elicited therapeutic antitumor responses in different tumor types by targeting distinct cathepsins with specific antibody–NNPI combinations.

Results

Design and development of NNPIs

Proteases of the cysteine cathepsin family present an enzymatic active site containing a Cys-His-Asn catalytic triad[1,4]. To develop covalent inhibitors that would block cysteine cathepsin activity, we designed NNPIs functionalized to react with the catalytic cysteine and form a covalent bond (Fig. 1a). We started from the octameric peptide LRMKLPKP extracted from the sequence of CD74, a specific substrate of CTSS[10,18], and used it as a template to introduce a Michael acceptor at four different positions to attempt to design a covalent inhibitor (Fig. 1b). The initial peptide sequence was further modified by adding a lysine at the N terminus for future functionalization and substituting the proline at the C terminus with an aspartate, as it increased the ability of the peptide to be bound by CTSS (Fig. 1b and Extended Data Fig. 1a). The Michael acceptor was positioned on the side chain of the amino acids at position P2 or P1′ (NNPI-1 or NNPI-2), in the backbone of the peptide substituting the lysine and leucine in P1 and P1′ (NNPI-3) or at the N terminus of a truncated version of the peptide (NNPI-4) (Fig. 1b). In particular, the NNPI-3 design was inspired by the result of docking the CD74 peptide into the CTSS structure (Protein Data Bank (PDB) 1NPZ)[50] using the Attracting Cavities docking software[51]. We found that the lysine and leucine at positions P1 and P1′ were situated in the vicinity of the reactive cysteine, providing the opportunity to replace them with a Michael acceptor to create a potential covalent ligand (Extended Data Fig. 1b). Using a fluorescence resonance energy transfer (FRET) assay, we tested the ability of any of these NNPIs to inhibit CTSS. We incubated purified CTSS protein with each NNPI and then added a peptide bearing a fluorescent dye as a substrate, with a quencher at the N and C termini; fluorescence emission over time was used as the readout of enzymatic activity. Only NNPI-3 reduced the protease activity (Fig. 1c and Extended Data Fig. 1c), albeit with low potency (half-maximal inhibitory concentration (IC_{50}) > 25 µM) (Extended Data Fig. 1d). To assess the specificity of NNPI-3, we tested it on a panel of five additional cathepsins. NNPI-3 also inhibited CTSB and CTSK but had no measurable activity against cathepsins H, Z and L (CTSH, CTSZ and CTSL; Fig. 1c). To improve the potency and specificity of NNPI-3, we designed a site saturation mutagenesis screening to determine the impact of every possible amino acid change on the potency of NNPI-3 when inhibiting CTSS and CTSB (Fig. 1d and Extended Data Fig. 3a). The library contained 126 NNPIs and we compared their activity relative to that of the original NNPI-3 (Fig. 1d). This unbiased screening revealed several amino acid changes that improved potency and specificity toward CTSS or CTSB. For example, a valine replacing the proline in position 5 (P5V) or different amino acids at positions 2 (L2F, L2H), 6 (K6F, K6L, K6M, K6W, K6Y) and 7 (D7F, D7W) strongly improved CTSS inhibition (Fig. 1d and Extended Data Fig. 1e). On the other hand, substitutions L2R, M4Y and P5W improved CTSB inhibition (Fig. 1d).

Next, we tested whether the combination of the single variants was additive and improved inhibition. Hence, we combined dual amino acid changes at positions 5, 6 and 7 and identified NNPI-C1 and NNPI-C2 as the best candidates for CTSS inhibition, improving the IC_{50} from >25 µM to 362.5 nM, a 68-fold improvement (Extended Data Fig. 1f,g). Then, we used NNPI-C2 and tested additional changes at positions 2 and 7 (L2F, L2H, D7Y and D7W) and identified NNPI-C10 as the most potent CTSS inhibitor (Fig. 1e and Extended Data Fig. 1h). NNPI-C10 inhibited the activity of CTSS (IC_{50} = 70.7 nM) and CTSB (IC_{50} = 117.0 nM) (Fig. 1e and Extended Data Fig. 1j). Subsequently, we used the screening information to further modify NNPI-C10 at positions 2, 4 and 5 and improved the specificity toward CTSB, thereby identifying NNPI-D5 as a highly specific inhibitor of CTSB (IC_{50} = 68.8 nM) (Fig. 1f and Extended Data Fig. 1i).

Then, we profiled NNPI-C10 and NNPI-D5 against five additional cathepsins and confirmed that NNPI-C10 selectively inhibited CTSS and partially inhibited CTSB, whereas NNPI-D5 was specific to CTSB (Extended Data Fig. 2a). Furthermore, we observed that NNPI-C10 also inhibited a mutant and overactive form of CTSS (CTSS Y132D;

Fig. 1 | Design and characterization of NNPIs. a, Overview of the three main steps of peptide design and antibody conjugation for targeted delivery of NNPIs. **b**, Structure of natural substrate and chemically modified peptides. The scissile bond is highlighted in red and the Michael acceptor is highlighted in pink. **c**, FRET assays testing the inhibitory activity of NNPI-3 on a panel of six cysteine cathepsins (n = 2 independent replicates). **d**, Site saturation mutagenesis screening and inhibition potency tested on CTSS and CTSB (n = 2 independent replicates). **e**,**f**, Dose–response curves quantifying the inhibitory potency in FRET assays of NNPI-C10 on CTSS (**e**) and NNPI-D5 on CTSB (**f**) (n = 3 independent replicates; mean and s.d. values are shown). A schematic representation of the structure of each NNPI is given below the corresponding graph. **g**, Mutagenesis screening and inhibition potency tested on CTSK and CTSL (n = 4 independent replicates). **h**,**i**, Dose–response curves quantifying the inhibitory potency in FRET assays of NNPI-F17 on CTSK (**h**) and NNPI-G14 on CTSL (**i**) (n = 3 independent replicates; mean and s.d. values are shown). A schematic representation of the structure of each NNPI is given below the corresponding graph.

https://doi.org/10.1038/s41589-024-01627-z

Extended Data Fig. 2b), which has been identified in 5% of patients diagnosed with follicular lymphoma[10], although we could not identify specific amino acid changes in NNPI-C10 to further improve selectivity toward CTSS Y132D (Extended Data Fig. 2c). Interestingly, while testing the selectivity of NNPIs on different cathepsins, we noticed that NNPI-D1 inhibited CTSK better than CTSS or CTSB; through selected single amino acid changes, we identified NNPI-E15 as a promising inhibitor of CTSK (Extended Data Fig. 2d-f). Hence, we used the sequence

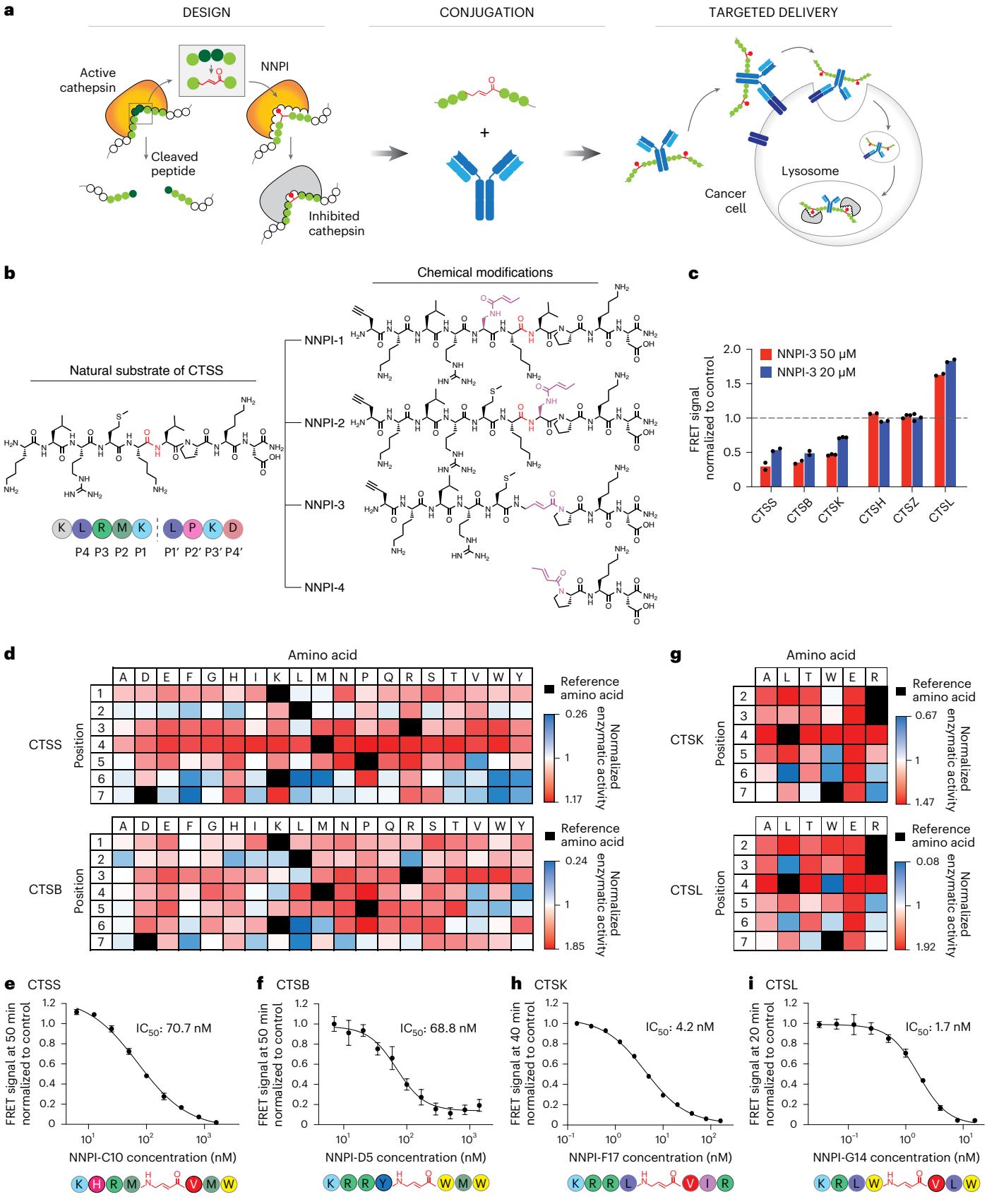

https://doi.org/10.1038/s41589-024-01627-z

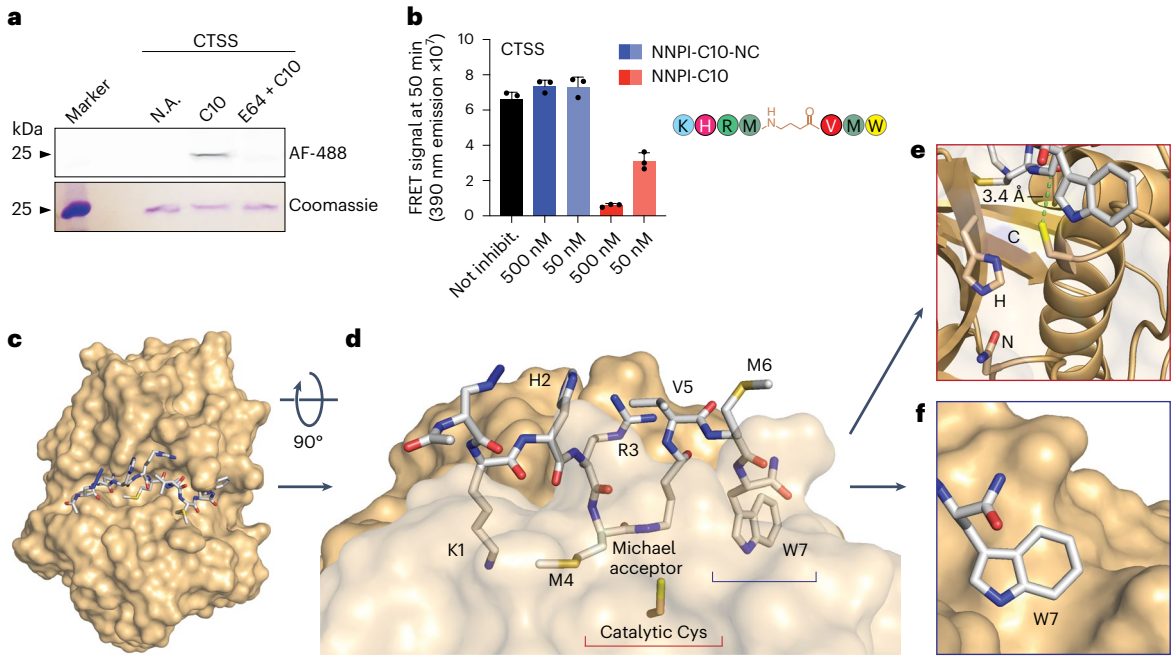

Fig. 2 | Covalent binding mode of NNPI-C10. a, Fluorescence and Coomassie blue staining of gel loaded with CTSS alone or incubated with E64 and/or AF488-derivatized NNPI-C10. Images from one of two independent experiments are presented. **b**, Results of FRET assay testing CTSS inhibition by NNPI-C10 and NNPI-C10-NC ($n = 3$ independent replicates; mean and s.d. values are shown). A schematic representation of NNPI-C10-NC is given on the right. **c**, Crystal structure of C10–CTSS Y132D complex. **d**, Loop conformation of NNPI-C10 in the substrate binding pocket of CTSS. **e**, Close distance (3.4 Å) between the Michael acceptor in NNPI-C10 (in white) and the catalytic cysteine of CTSS (in yellow), consistent with the expected covalent bond formation. **f**, The terminal tryptophan of NNPI-C10 engages a hydrophobic cavity of CTSS.

of NNPI-E15 as a starting point to create a second NNPI library ($n = 32$ NNPIs) to determine the impact of each amino acid type (that is, small, apolar, polar, aromatic, negatively charged or positively charged) at different positions when inhibiting CTSK and CTSL (Extended Data Fig. 3b). In the first screening, we identified and confirmed four promising amino acid changes for CTSK (V5W, M6L, M6W and W7R) and CTSL (R3L, L4W, M6L and W7T) (Fig. 1g and Extended Data Fig. 3c,d). Next, we tested alternative changes at positions 3, 4, 5, 6 and 7 and noticed that V5Y and M6I improved potency on CTSK while L4Y, V5H and M6I were better changes for CTSL inhibition (Extended Data Fig. 3e,f). In the last step, we combined the best variants, although we selected L4W instead of L4Y for the CTSL inhibitor, as Y4 would have increased the affinity for CTSB (Fig. 1d), and M6L was preferred to M6I, as the latter also improved inhibition of CTSK (Extended Data Fig. 3e).

Interestingly, for CTSK, the combination yielding the strongest inhibition was not that in which all promising amino acid changes were implemented; two changes at positions 6 and 7 were sufficient to identify NNPI-F17 as the best CTSK inhibitor ($IC_{50} = 4.2$ nM) (Fig. 1h and Extended Data Fig. 3g), suggesting that the effects of these changes were not purely additive. For CTSL, the combination of W4, L3 and M6 in NNPI-G12 yielded to the most potent inhibitor (Extended Data Fig. 3h). However, given its poor solubility and the similar potency of NNPI-G14, we selected the latter as the best CTSL inhibitor ($IC_{50} = 1.7$ nM) (Fig. 1i and Extended Data Fig. 3h). Lastly, we confirmed the specificity for CTSK and CTSL of these two NNPIs on the panel of seven cysteine cathepsins (Extended Data Fig. 2a). Overall, using a stepwise rational design and screening approach, we identified four potent NNPIs with distinct specificities for CTSS, CTSB, CTSK and CTSL.

Covalent binding mode of NNPIs

To demonstrate the covalent inhibition mode of NNPI-C10, we incubated purified CTSS protein with NNPI-C10 functionalized with a fluorophore (Alexa Fluor 488 (AF488)) and used SDS–PAGE to assess the formation of the adduct. As a control, we used E64, a generic small-molecule covalent inhibitor of cysteine proteases, which would prevent NNPI-C10 binding. Gel-based image analyses revealed a fluorescent band at the expected molecular mass of CTSS (25 kDa) when the enzyme was incubated with $NNPI\text{-}C10^{AF488}$ but not in the E64 preincubated sample (Fig. 2a). Conversely, when $NNPI\text{-}C10^{AF488}$ was coincubated with CTSS and E64 was added later to the mix at increasing concentrations, the CTSS–C10 complex was still detectable, indicating that the NNPI could not be displaced and, thus, confirming the formation of a covalent bond (Extended Data Fig. 4a). Moreover, we modified NNPI-C10 by replacing the double bond in the Michael acceptor with a single bond to abrogate its ability to covalently block CTSS activity (Extended Data Fig. 4b). Indeed, incubation of CTSS with this chemically modified version of NNPI-C10 did not affect CTSS activity (Fig. 2b). Lastly, we used intact mass spectrometry analysis in denaturing conditions to further confirm that a covalent bond was formed between CTSS and the NNPI. A peak corresponding to the sum of the molecular masses of CTSS and NNPI-C10 (27,016.701 Da) was observed (Extended Data Fig. 4c), demonstrating that NNPI-C10 is a covalent inhibitor.

Next, to characterize the binding mode of NNPI-C10 to CTSS, we obtained the crystal structure of NNPI-C10 in complex with CTSS wild type (WT) and Y132D (Supplementary Table 1). We compared the structures of CTSS WT and Y132D; although the Y132D substitution increases the catalytic activity[10], no notable structural change was observed and the NNPI-C10 binding mode was similar for both variants (Extended Data Fig. 5a,b). Analyses of the NNPI-C10–CTSS complex structure confirmed the binding of NNPI-C10 in the catalytic pocket as expected from the substrate's binding mode, with the Michael acceptor correctly positioned to form a covalent bond with the catalytic C139 (Fig. 2c,d). Distinctly from other CTSS–ligand complex structures[52], NNPI-C10 in the bound state did not adopt a fully extended conformation; instead, it presented a turn configuration at positions 5 and 6 (Fig. 2d). This conformation allowed the Michael acceptor to reach

the active cysteine (Fig. 2e) and enabled an interaction between W7 of NNPI-C10 and a hydrophobic cavity at the edge of the enzyme's catalytic pocket (Fig. 2f). In addition, rationalizing the results of the mutagenesis screens in light of the crystal structures suggested that the preferred aromatic amino acids at positions 2 and 7 likely established interactions with F184 of CTSS (Extended Data Fig. 5c) and F260 or W300 of CTSS (Extended Data Fig. 5d), respectively. Moreover, we observed the presence of five hydrogen bonds between NNPI-C10 and CTSS (Extended Data Fig. 5e), involving R3 and M4. In this regard, we also noticed that M4 appeared to be essential because all possible substitutions were found to be detrimental (Fig. 1d). Overall, from the crystal structures, we could confirm that the NNPIs block the catalytic site of cathepsins; through extensive biochemical characterization, we also confirmed that such inhibition occurs in a covalent fashion.

Antibody-mediated delivery of NNPIs to cancer cells

Peptide-based drugs are known to have poor membrane permeability and a short half-life in vivo[53–55]. To overcome these limitations and specifically deliver NNPIs to tumor cells, we designed antibody-peptide inhibitor conjugates (APIC) (Fig. 3a). Using maleimide chemistry, we conjugated NNPI-C10 with anti-CD22 (epratuzumab) or anti-CD79 antibodies to target B cell lymphoma, as CTSS is an oncogenic driver in this tumor[10]. Additionally, NNPI-D5 was conjugated with an anti-HER2 (human epidermal growth factor receptor 2) antibody (trastuzumab) to target breast cancer cells and block CTSB activity in solid tumors, while NNPI-F17 and NNPI-G14 were conjugated with an anti-SIGLEC-15 (sialic acid-binding Ig-like lectin 15) antibody to target osteoclasts or cancer cells and inhibit CTSK and CTSL, respectively. First, we observed using intact mass spectrometry that antibodies were conjugated with a variable number of NNPIs (Fig. 3b and Extended Data Fig. 6a). Then, CTSS was coincubated with APICs and mass photometry analyses revealed that NNPIs did not need to be released from the antibody to bind CTSS because we detected the formation of CTSS–APIC complexes (Fig. 3c). The number of CTSS molecules bound to each APIC increased proportionally to the number of NNPIs conjugated (Fig. 3c and Extended Data Fig. 6b), confirming that NNPIs can bind their target even in the absence of antibody degradation.

To further investigate the ability of CTSS of binding to APICs in solution, we coincubated activated histidine-tagged CTSS (molecular mass = 25 kDa) with the anti-CD79–C10 APIC and we used the protease inhibitor E64 as a control to prevent binding. Western blot analysis confirmed the formation of the APIC–CTSS complexes, as demonstrated by the presence of multiple specific bands at different molecular masses, indicating binding of one or multiple CTSS molecules to the APIC light chain (band at ~50 kDa) or heavy chain (bands at ~75 kDa and higher) (Fig. 3d). Overall, in vitro assays showed that APICs retained the ability to bind and block cathepsin activity. Next, we tested the activity of APICs in cellular assays to assess binding to cell receptors, internalization, accumulation in the lysosomes and inhibition of their specific targets. We used lymphoma cells (WSU-DLCL2 and Raji) expressing high levels of CD22 and CD79 and breast cancer cells (BT-474 and HCC-1569) expressing HER2 (Extended Data Fig. 6c,d). First, APICs were conjugated with a fluorophore (AF488); by flow cytometry (FC), we observed that they retained the ability to bind to the surface receptor (Fig. 3e). Then, we used a quencher to block the APIC fluorescence signal on the cell surface but not in the cytoplasm. In cells maintained in physiological condition (37 °C), the majority of the fluorescence signal was retained, indicating that most of the APIC was internalized. Conversely, in cells at low temperature (4 °C) where receptor–ligand internalization was slowed down, most of the APICs bound to the receptor remained on the cell surface; thus, the fluorescence signal was quenched (Fig. 3e and Extended Data Fig. 6e). Next, to test the accumulation of APICs in the acidic endosomes and lysosomes, we used a pH-sensitive dye that is highly fluorescent only in acidic environments (pHrodo). Here, we observed a specific increase in fluorescence signal in lymphoma and breast cancer cells in physiological condition compared to 4 °C (Fig. 3f), indicating that APICs accumulated in the endolysosomal compartment upon internalization.

Lastly, we used a pan-cathepsin quenched activity-based probe (qABP, named BMV109)[56–58] to determine the ability of different APICs to inhibit their targets in cells, while small-molecule inhibitors (petesicatib, E64, odanacatib and Z-FY-CHO) were used as controls[32,35,59,60]. The BMV109 probe is fluorescent only after reacting with a cathepsin, which allows an assessment of protease activity. Treatment of lymphoma and primary B cells with anti-CD79–C10, breast cancer cells with anti-HER2–D5, osteoclasts with anti-SIGLEC-15–F17 and prostate cancer cells with anti-SIGLEC-15–G14 prevented the binding of the qABP to the specific cathepsin and the fluorescent band at the expected molecular mass disappeared (Fig. 3g–j and Extended Data Fig. 7a–c). A dose-dependent treatment experiment clearly showed that the fluorescence signal intensity of qABP was inversely proportional to the inhibition of the given cathepsin (Extended Data Fig. 7d). In summary, antibody-mediated delivery of NNPIs promotes cellular internalization and efficient inhibition of the catalytic activity of endogenous cysteine proteases in cancer cells.

APIC inhibition of CTSS induces antitumoral immune response

Cathepsins regulate various biological processes and, despite partial functional redundancy, some cathepsins have a specialized role in specific cellular contexts. CTSS has the nonredundant activity of cleaving the chaperone protein CD74 in the lysosome[18]. Indeed, genetic KO of *CTSS* in lymphoma cells induced the accumulation of CD74 (Fig. 4a), impairing the maturation of MHC-II and altering the interaction between lymphoma cells and T cells[10]. Thus, we tested whether treatment with APICs (anti-CD79–C10 or anti-CD22–C10) could recapitulate the phenotype observed in *CTSS* KO cells. Lymphoma cells treated with anti-CD22–C10 showed a dose-dependent accumulation of CD74, exceeding the levels that we could detect in cells treated with petesicatib (a specific CTSS inhibitor) at higher concentrations (Fig. 4b). A similar effect was observed in lymphoma cells treated with anti-CD79–C10 (Extended Data Fig. 8a,b) or in cells expressing the mutant and overactive form of CTSS (Extended Data Fig. 8c). Interestingly, the combination treatment at low doses with APICs targeting different receptors (CD22 and CD79) induced the accumulation of CD74 similar to the level seen for treatment with individual APICs at high doses (Fig. 4c), suggesting that combinations of antibodies targeting different receptors can be used to efficiently deliver NNPIs to tumor cells. In lymphomas, loss of CTSS activity and accumulation of CD74 lead to alterations in antigen presentation, which allow the recognition of tumor cells by $CD8^+$ cytotoxic T cells and the activation of an antitumoral response. However, this therapeutic immune response could not be observed using small-molecule inhibitors targeting cysteine proteases[10]. Hence, we tested whether treatment with APICs could overcome this limitation. To determine cytotoxic $CD8^+$ T cell activation upon APIC treatment, we performed an antigen-based coculture assay using mouse $CD8^+$ T cells and lymphoma cells. We verified that NNPI-C10, designed to block human CTSS, was able to inhibit the mouse Ctss (Extended Data Fig. 8d,e) and that treatment with the mouse APIC (anti-mouse CD79–C10) induced CD74 accumulation in mouse cells, as observed in the human counterpart (Extended Data Fig. 9a). Notably, in coculture assays, treatment with APICs induced the robust proliferation of $CD8^+$ T cells (Fig. 4d–f and Extended Data Fig. 9b,c) and killing of cancer cells (Fig. 4g), fully recapitulating the phenotype that could be observed using *CTSS* KO cells. Importantly, activation of $CD8^+$ T cells could only be achieved upon treatment with APIC but not with a small-molecule inhibitor of CTSS such as petesicatib (Fig. 4e,f and Extended Data Fig. 9b,c).

Moreover, we could demonstrate that the activation of $CD8^+$ T cells is directly linked to a loss of CTSS activity and alteration in antigen presentation mediated by MHC-I in lymphoma cells because APIC

https://doi.org/10.1038/s41589-024-01627-z

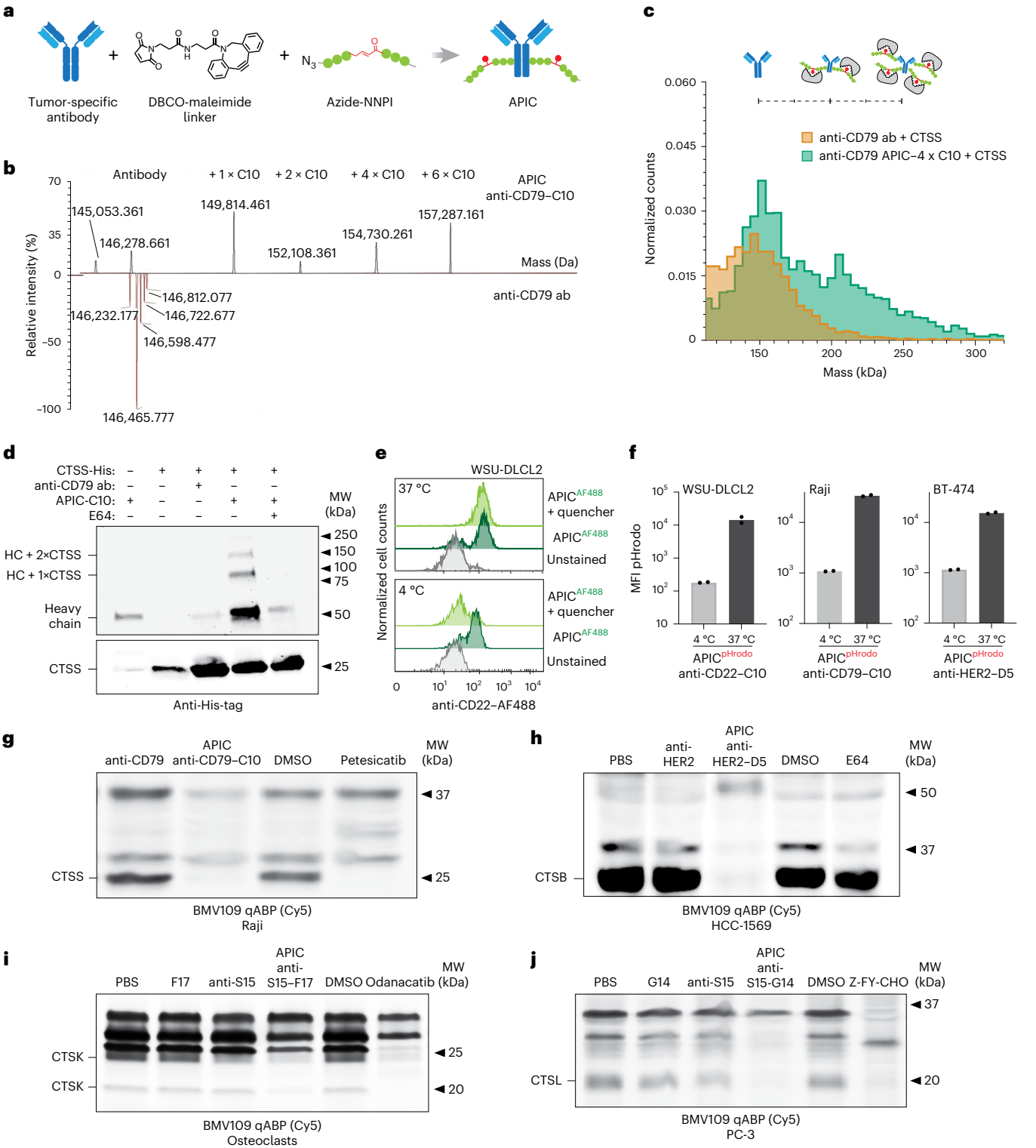

Fig. 3 | Antibody conjugation of NNPIs and functional delivery in different tumor cells to inhibit specific cathepsins. a, Antibody conjugation strategy with an NNPI through two sequential chemical reactions, mediated by a molecular linker (DBCO-maleimide). **b**, Intact mass spectrometry analysis of the anti-CD79–C10 APIC (black peaks) compared to the unconjugated anti-CD79 antibody (red peaks). **c**, Mass photometry analysis of anti-CD79 antibody (yellow) or anti-CD79–C10 APIC (green) mixed with CTSS. **d**, Western blot analysis of His-tagged recombinant CTSS alone or mixed with APIC or control antibody. In the control condition, CTSS was preincubated with E64 (last lane). Anti-His antibody was used for CTSS detection. Blots from one of two independent experiments are presented. **e**, Representative FC analysis of WSU-DLCL2 lymphoma cells stained with AF488-labeled APICs in different conditions at 37 °C and 4 °C ($n = 2$ per condition). **f**, Quantification of pHrodo fluorescence upon internalization and accumulation in the endolysosomal compartment of the anti-CD22–C10, anti-CD79–C10 and anti-HER2–D5 APICs ($n = 2$ per condition). **g**, CTSS inhibition in Raji cells treated with the anti-CD79–C10 APIC or petesicatib, assessed by a BMV109 qABP. **h**, CTSB inhibition in HCC-1569 breast cancer cells, assessed by BMV109 qABP. **i**, CTSK inhibition in human osteoclasts, assessed by BMV109 qABP. **j**, CTSL inhibition in PC-3 prostate cancer cells, assessed by BMV109 qABP. Images corresponding to additional replicates of the experiments performed with the BMV109 probe are reported in Extended Data Fig. 7.

treatment in *B2M* KO cells with impaired formation of MHC-I was not able to activate CD8$^+$ T cells (Fig. 4e,f and Extended Data Fig. 9d). Strikingly, these results indicate that targeting CTSS exclusively in B cells is essential to elicit the full therapeutic potential of this target and APICs can be used to achieve this goal.

APIC-mediated inhibition of CTSB hinders tumor invasiveness

In solid tumors, the intracellular and extracellular activity of cysteine proteases regulates many aspects of cancer biology[2,3]. In particular, high levels of CTSB have been associated with tumor progression and metastasis in the context of multiple malignancies, including breast cancer[16,19,20]. Thus, we tested whether the anti-HER2–D5 APIC targeting CTSB in HER2$^+$ breast cancer cells could prevent cell migration and invasion. Treatment of two independent breast cancer cell lines (BT-474 and HCC-1569) with APICs showed a significant decrease in cell migration using a Matrigel-based experimental setup (Fig. 4h–j), while the anti-HER2 antibody, NNPI-D5 alone or an unconjugated mix of anti-HER2 and NNPI-D5 did not induce the same effect (Fig. 4h–j). In addition, HCC-1569 cells are reported to be resistant to trastuzumab[61]; indeed, treatment with anti-HER2 antibody or the APIC with D5 did not affect cell viability or proliferation (Extended Data Fig. 9e), indicating that the effect on cell migration can be specifically attributed to intracellular CTSB inhibition and that treatment with anti-HER2–D5 represents an efficient way to block its activity. Overall, using a modular combination of NNPIs and antibodies, we were able to achieve and exploit targeted NNPI delivery to block the activity of specific cathepsins and inhibit key oncogenic processes in B cell lymphoma and breast cancer.

APIC therapeutic efficacy in vivo

To evaluate the therapeutic potential of APICs in vivo, we used preclinical xenografts and transgenic animal models and assessed the ability of the anti-CD79–C10 APIC to accumulate in cancer cells, block CTSS activity and induce antitumoral immune responses. To determine the in vivo biodistribution and pharmacokinetics of APICs, we performed positron-emission tomography (PET) imaging and biodistribution studies with [^{64}Cu]-APIC. Specific accumulation of [^{64}Cu]-APIC was detected in the tumor mass 48 h after injection but not in other organs (Fig. 5a,b) or circulating in the peripheral blood (Fig. 5c), while we observed that the radioactive signal from the tumor decreased in animals injected with [^{64}Cu]-APIC together with an excess of unlabeled APIC, indicating that labeled and unlabeled APICs were competing for the same receptor on tumor cells. Similar results were obtained in independent biodistribution experiments using [^{111}In]-APIC at 48 h and 72 h after injection (Extended Data Fig. 10a–d).

Next, we directly measured cathepsin activity in lymphoma-bearing mice by systemic injection of qABP BMV109 (Fig. 5d) and we detected a clear reduction in fluorescence signal intensity in animals treated with APICs or in *CTSS* KO tumors compared to the untreated animals (Fig. 5e,f). Altogether, these results indicate that, in preclinical models using human cancer cells, we specifically delivered APICs to the tumor and inhibited the target activity. Lastly, because inhibition of CTSS induces antitumoral immune responses mediated by activated cytotoxic CD8$^+$ T cells, to fully assess the efficacy of APIC treatment in vivo, we needed an immunocompetent model. To that end, we selected VavP-*Bcl2* transgenic animals, which spontaneously develop follicular lymphoma, an indolent form of B cell malignancy, and whose tumors recapitulate key pathological features of the human disease[62]. Notably, animals treated with the anti-mouse CD79–C10 APIC biweekly for 3 weeks showed a significant decrease in B220$^+$ B cells, in correlation with an increase in antitumoral cytotoxic CD8$^+$ T cells (Fig. 5g–j and Extended Data Fig. 10e,f). Detailed multicolor immunofluorescence tissue analysis and relative quantification clearly detected a reduction in B220$^+$ lymphoma cells (blue) and CD4$^+$ T cells (green) and an increase in CD8$^+$ T cells (red) in APIC-treated animals (Fig. 5i–l), fully recapitulating the phenotype observed in VavP-*Bcl2 CTSS* KO mice[10] (Fig. 5i–l and Extended Data Fig. 10g). The overall fraction of cells in the hematopoietic compartment was not impacted by APIC treatment and treated mice did not lose weight compared to those treated with unconjugated antibody (Extended Data Fig. 10h,i), indicating good tolerability of the treatment. Overall, we demonstrated that, using a modular combination of antibodies and NNPIs, we can tailor the design of APICs to block specific oncogenic cysteine proteases in vivo.

Discussion

The structure and mechanism of action of a protein can be used as the starting point to rationally design specific inhibitors[63,64]. In this study, we took advantage of the conserved catalytic pocket of cysteine cathepsins to design covalent inhibitors and develop a screening platform for the rapid identification of selective inhibitors targeting different cathepsins. Remarkably, using site saturation mutagenesis screenings, we rapidly improved NNPI potency and achieved specificity. This represents a notable advantage compared to more classical medicinal chemistry approaches that require the laborious modifications of several chemical groups of the original small molecule to improve its potency. Cathepsins have evolved to recognize specific peptide sequences and have different substrate selectivity. The screening strategy that we adopted efficiently explores and exploits the different substrate preferences of each protease, facilitating the identification of specific inhibitors. With this approach, it is also possible to develop NNPIs with a broader reactivity to multiple cathepsins, if necessary. Indeed, the possibility to modulate the design of NNPIs to inhibit one or multiple targets could become useful to anticipate problems of redundancy in cathepsin activity and to prevent compensatory mechanisms by other proteases. Here, starting from rational design, we developed covalent and specific cathepsin inhibitors; however, in the future, our approach could be extended to other cysteine, threonine or serine proteases using similar principles[65].

To be therapeutically effective and limit side effects, inhibitors not only need to selectively bind their target but must also reach the desired cells. To this purpose, we exploited a cell-type-specific delivery modality that also improves NNPI stability and internalization and we demonstrated that conjugation with therapeutic antibodies is ideal for the delivery of NNPIs to inhibit cathepsins. The activity of cathepsins is required in the lysosome for protein degradation and recycling. APICs accumulating in the lysosome could be subjected to cathepsin-mediated degradation; however, NNPIs are able to bind cathepsins even while attached to the antibodies, forming APIC–cathepsin complexes. Thus, APICs seem to act as molecular traps for cathepsins. Moreover, a targeted delivery approach appears to be essential to maximize the therapeutic impact of cathepsin inhibition. In fact, several cysteine cathepsins are validated targets for treating various diseases. However, in clinical trials, systemic inhibition of specific cathepsins such as CTSK and CTSS using small-molecule inhibitors has resulted in either inefficacy or harmful side effects. This led to the withdrawal of a CTSK inhibitor from the market[5,40–42] and hampered the interest in advancing the development of cathepsin inhibitors. We tested the efficacy of petesicatib, a small-molecule inhibitor targeting CTSS, and our APIC in parallel. Notably, inhibition of CTSS activity could be achieved with both compounds but only the treatment with the APIC was able to induce the activation of cytotoxic CD8$^+$ T cells, triggering the killing of tumor cells. We also demonstrated that our modular drug platform can be used to develop APICs for the treatment of other diseases such as osteoporosis by targeting osteoclasts; the same could be achieved for autoimmune disorders by tailoring the combination of NNPIs and antibodies. Considering that cathepsins regulate several physiological processes and are expressed in most cell types, cell-type-specific delivery of the inhibitor represents an exquisite opportunity to therapeutically block the activity of these proteases while preventing side effects, reviving the possibility of using cathepsin inhibitors in the

https://doi.org/10.1038/s41589-024-01627-z

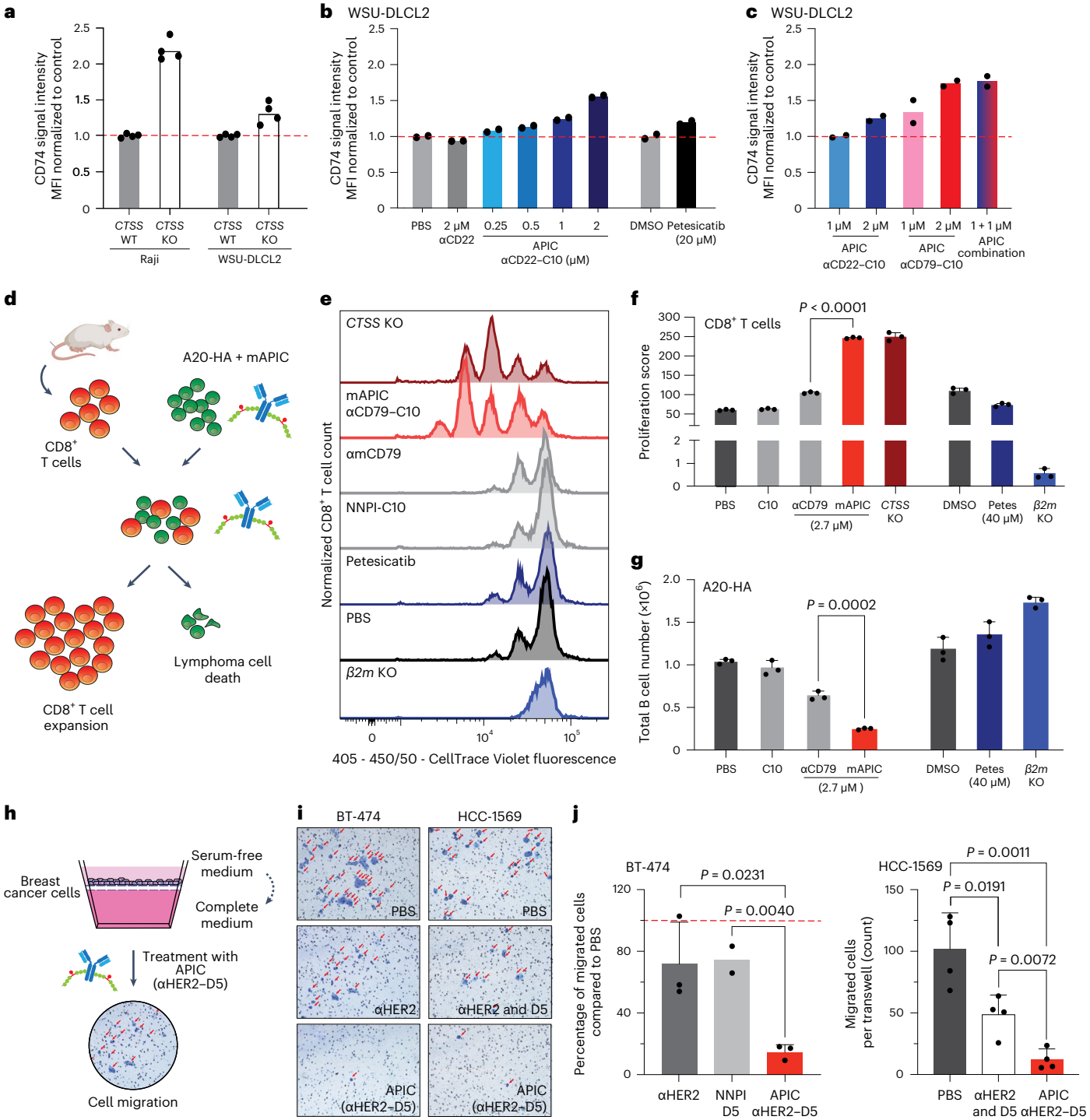

Fig. 4 | Treatment with APICs modulates tumor antigen presentation, induces lymphoma cell killing by CD8⁺ T cells and hinders tumor invasion in vitro. a, Quantification of CD74 accumulation detected by FC in Raji and WSU-DLCL2 cells with CTSS WT (gray) or *CTSS* KO (white). Median fluorescence intensity (MFI) is normalized to the CTSS WT condition ($n = 4$ independent wells analyzed per condition). **b**, Quantification of CD74 accumulation detected by FC in WSU-DLCL2 cells after 48-h incubation in the indicated conditions. MFI is normalized to the PBS condition ($n = 2$ independent wells treated per condition). **c**, Quantification of CD74 accumulation detected after 48-h incubation with anti-CD22 APIC (blue), anti-CD79 APIC (red) or a combination of the two APICs (blue–red). Data are normalized to the samples treated with 2 μM unconjugated anti-CD22 antibody ($n = 2$ independent wells treated per condition). **d**, Scheme of T cell assay performed with CD8⁺ T cells isolated from a CL4 TCR mouse and A20 lymphoma cells expressing *HA*. **e**–**g**, Representative proliferation peaks (**e**) and proliferation score (**f**) of CD8⁺ T cells and total number of A20 lymphoma cells (**g**) after 72 h of coculture in the indicated conditions ($n = 3$ independent wells treated per condition; mean and s.d. values are shown). *P* values were determined by a two-tailed *t*-test. **h**, Scheme of invasion assay with breast cancer cell lines. **i**, Representative images of sampled regions of stained membranes. **j**, Quantification of cell migration based on imaging of stained membranes in the indicated conditions in BT-474 (three separate experiments, each with $n = 3$ independent transwells treated per condition; mean and s.e.m. values are shown) and HCC-1569 ($n = 4$ independent transwells treated per condition; mean and s.d. values are shown) breast cancer cells. *P* values were determined by a two-tailed *t*-test.

https://doi.org/10.1038/s41589-024-01627-z

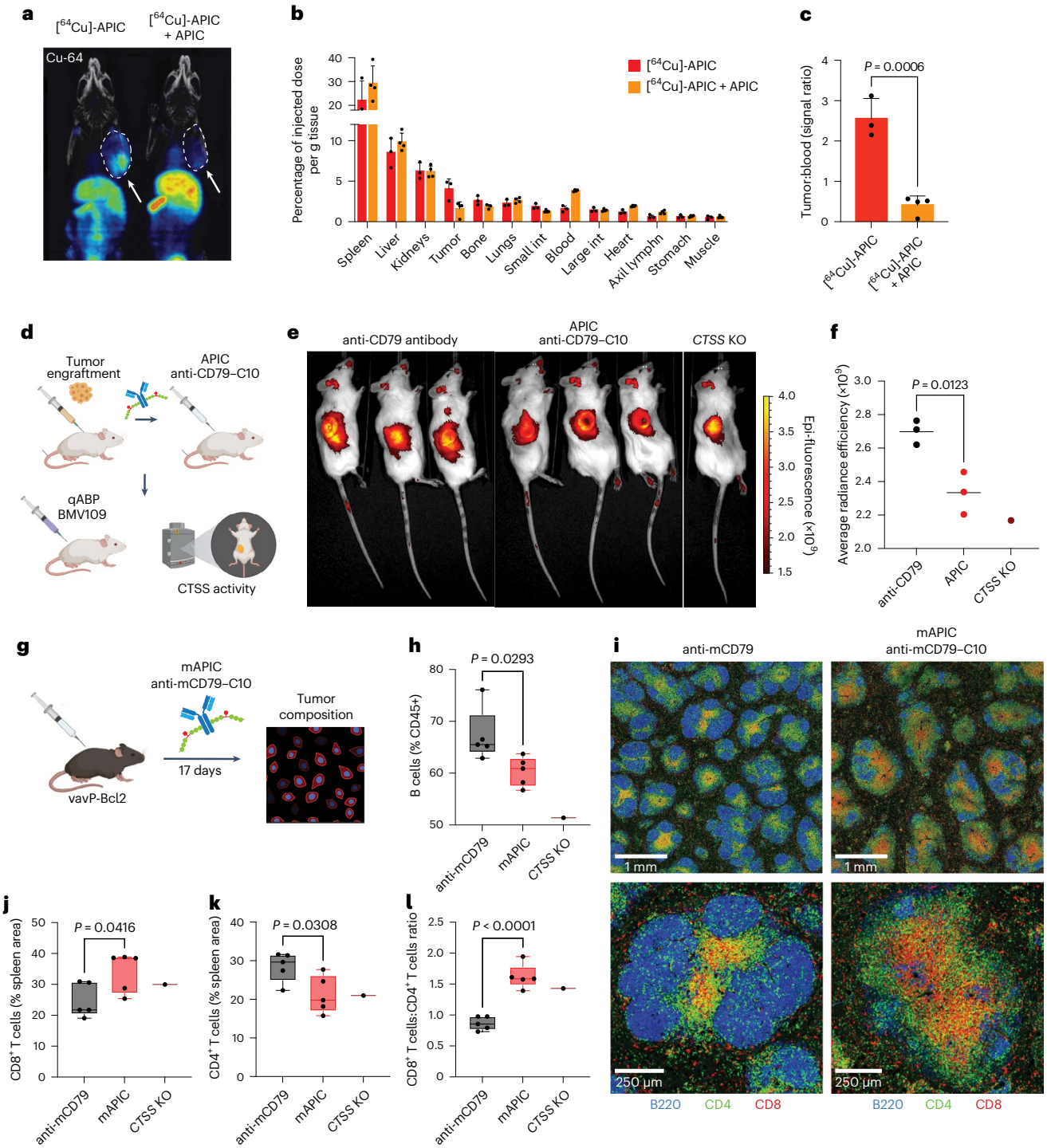

Fig. 5 | Treatment with APICs induces antitumoral response in vivo. **a**, Representative image of fused coronal PET–CT (computed tomography) 48 h after injection of [^{64}Cu]-APIC in NSG mice bearing Raji subcutaneous tumors. Tumor mass is indicated by a white arrow ($n = 2$ per condition). **b**, Biodistribution of [^{64}Cu]-APIC in tumor-bearing mice in the presence (orange bars; $n = 4$) or absence (red bars; $n = 3$; mean and s.d. values are shown) of an excess of unlabeled APIC. **c**, Tumor-to-blood ratios computed for the biodistribution experiment in the presence (orange bars; $n = 4$) or absence (red bars; $n = 3$; mean and s.d. values are shown) of an excess of unlabeled APIC. **d**, Scheme of in vivo experiment for the imaging of cathepsin activity. **e**, Fluorescence images of mice 8 h after injection of BMV109 probe. **f**, Quantification of fluorescence signal radiating from tumor mass ($n = 3$ mice per group). Bars represent the mean for each group. The *P* value was determined by a two-tailed *t*-test. **g**, Scheme of in vivo experiment on VavP-*Bcl2* mouse model of B cell lymphoma. **h**, FC quantification of B cells in the spleen of mice treated with the APIC (red) or unconjugated anti-mouse CD79 antibody (gray) ($n = 5$ mice per group). A *CTSS* KO mouse (dark red) was included as a reference. The central line of the box plots indicates the median value, the whiskers indicate the maximum and minimum values and the box limits correspond to the 25th and 75th percentiles. The *P* value was determined by a two-tailed *t*-test. **i**–**l**, Representative images of multicolor immunofluorescence (**i**) and quantification of CD8$^+$ T cells (j), CD4$^+$ T cells (k) and CD8$^+$–CD4$^+$ T cell ratio (**l**) in the spleens of mice treated with the APIC (red) or unconjugated anti-mouse CD79 antibody (gray) ($n = 5$ mice per group). A *CTSS* KO mouse (dark red) was included as a reference. The central line of the box plots indicates the median value, the whiskers indicate the maximum and minimum values and the box limits correspond to the 25th and 75th percentiles. *P* values were determined by a two-tailed *t*-test.

clinic for the treatment of cancers and other diseases. The development of analogous cell-type-specific inhibition strategies might prove effective to target other proteases that are involved in several different pathological conditions, opening the way to a generation of targeted therapies with cell-type-specific delivery.

Online content

Any methods, additional references, Nature Portfolio reporting summaries, source data, extended data, supplementary information, acknowledgements, peer review information; details of author contributions and competing interests; and statements of data and code availability are available at https://doi.org/10.1038/s41589-024-01627-z.

References

1. Turk, V. et al. Cysteine cathepsins: from structure, function and regulation to new frontiers. *Biochim. Biophys. Acta Proteins Proteom.* **1824**, 68–88 (2012).
2. Olson, O. C. & Joyce, J. A. Cysteine cathepsin proteases: regulators of cancer progression and therapeutic response. *Nat. Rev. Cancer* **15**, 712–729 (2015).
3. Vidak, E., Javoršek, U., Vizovišek, M. & Turk, B. Cysteine cathepsins and their extracellular roles: shaping the microenvironment. *Cells* **8**, 264 (2019).
4. Novinec, M. & Lenarčič, B. Papain-like peptidases: structure, function, and evolution. *Biomol. Concepts* **4**, 287–308 (2013).
5. McClung, M. R. et al. Odanacatib for the treatment of postmenopausal osteoporosis: results of the LOFT multicentre, randomised, double-blind, placebo-controlled trial and LOFT Extension study. *Lancet Diabetes Endocrinol.* **7**, 899–911 (2019).
6. Smyth, P., Sasiwachirangkul, J., Williams, R. & Scott, C. J.Cathepsin S (CTSS) activity in health and disease—a treasure trove of untapped clinical potential. *Mol. Aspects Med.* **88**, 101106 (2022).
7. Costa, A. G., Cusano, N. E., Silva, B. C., Cremers, S. & Bilezikian, J. P. Cathepsin K: its skeletal actions and role as a therapeutic target in osteoporosis. *Nat. Rev. Rheumatol.* **7**, 447–456 (2011).
8. McGlinchey, R. P. & Lee, J. C. Cysteine cathepsins are essential in lysosomal degradation of α-synuclein. *Proc. Natl Acad. Sci. USA* **112**, 9322–9327 (2015).
9. Fonović, M. & Turk, B. Cysteine cathepsins and extracellular matrix degradation. *Biochim. Biophys. Acta Gen. Subj.* **1840**, 2560–2570 (2014).
10. Dheilly, E. et al. Cathepsin S regulates antigen processing and T cell activity in non-Hodgkin lymphoma. *Cancer Cell* **37**, 674–689 (2020).
11. Bararia, D. et al. Cathepsin S alterations induce a tumor-promoting immune microenvironment in follicular lymphoma. *Cell Rep.* **31**, 107522 (2020).
12. Rao, J. S. Molecular mechanisms of glioma invasiveness: the role of proteases. *Nat. Rev. Cancer* **3**, 489–501 (2003).
13. Lah, T. T. & Kos, J. Cysteine proteinases in cancer progression and their clinical relevance for prognosis. *Biol. Chem.* **379**, 125–130 (1998).
14. Sevenich, L. et al. Analysis of tumour- and stroma-supplied proteolytic networks reveals a brain-metastasis-promoting role for cathepsin S. *Nat. Cell Biol.* **16**, 876–888 (2014).
15. Gocheva, V. et al. Distinct roles for cysteine cathepsin genes in multistage tumorigenesis. *Genes Dev.* **20**, 543–556 (2006).
16. Gopinathan, A. et al. Cathepsin B promotes the progression of pancreatic ductal adenocarcinoma in mice. *Gut* **61**, 877–884 (2012).
17. Shi, G. P. et al. Human cathepsin S: chromosomal localization, gene structure, and tissue distribution. *J. Biol. Chem.* **269**, 11530–11536 (1994).
18. Riese, R. J. et al. Essential role for cathepsin S in MHC class II-associated invariant chain processing and peptide loading. *Immunity* **4**, 357–366 (1996).
19. Victor, B. C., Anbalagan, A., Mohamed, M. M., Sloane, B. F. & Cavallo-Medved, D. Inhibition of cathepsin B activity attenuates extracellular matrix degradation and inflammatory breast cancer invasion. *Breast Cancer Res.* **13**, R115 (2011).
20. Heidtmann, H.-H., Salge, U., Abrahamson, M., Ben, M. & Kastelic, L.Cathepsin B and cysteine proteinase inhibitors in human lung cancer cell lines. *Clin. Exp. Metastasis* **15**, 368–381 (1997).
21. Niedergethmann, M. et al. Prognostic impact of cysteine proteases cathepsin B and cathepsin L in pancreatic adenocarcinoma. *Pancreas* **29**, 204–211 (2004).
22. Nouh, M. A. et al. Cathepsin B: a potential prognostic marker for inflammatory breast cancer. *J. Transl. Med.* **9**, 1 (2011).
23. Fujise, N. et al. Prognostic impact of cathepsin B and matrix metalloproteinase-9 in pulmonary adenocarcinomas by immunohistochemical study. *Lung Cancer* **27**, 19–26 (2000).
24. Sudhan, D. R., Pampo, C., Rice, L. & Siemann, D. W. Cathepsin L inactivation leads to multimodal inhibition of prostate cancer cell dissemination in a preclinical bone metastasis model. *Int. J. Cancer* **138**, 2665–2677 (2016).
25. Le Gall, C. et al. A cathepsin K inhibitor reduces breast cancer induced osteolysis and skeletal tumor burden. *Cancer Res.* **67**, 9894–9902 (2007).
26. Podgorski, I., Linebaugh, B. E. & Sloane, B. F. Cathepsin K in the bone microenvironment: link between obesity and prostate cancer? *Biochem. Soc. Trans.* **35**, 701–703 (2007).
27. Choe, Y. et al. Substrate profiling of cysteine proteases using a combinatorial peptide library identifies functionally unique specificities. *J. Biol. Chem.* **281**, 12824–12832 (2006).
28. Biniossek, M. L., Nägler, D. K., Becker-Pauly, C. & Schilling, O. Proteomic identification of protease cleavage sites characterizes prime and non-prime specificity of cysteine cathepsins B, L, and S. *J. Proteome Res.* **10**, 5363–5373 (2011).
29. Baugh, M. et al. Therapeutic dosing of an orally active, selective cathepsin S inhibitor suppresses disease in models of autoimmunity. *J. Autoimmun.* **36**, 201–209 (2011).
30. Saegusa, K. et al. Cathepsin S inhibitor prevents autoantigen presentation and autoimmunity. *J. Clin. Invest.* **110**, 361–369 (2002).
31. Lee-Dutra, A., Wiener, D. K. & Sun, S. Cathepsin S inhibitors: 2004–2010. *Expert Opin. Ther. Pat.* **21**, 311–337 (2011).
32. Theron, M. et al. Pharmacodynamic monitoring of RO5459072, a small molecule inhibitor of cathepsin S. *Front. Immunol.* **8**, 806 (2017).
33. Payne, C. D. et al. Pharmacokinetics and pharmacodynamics of the cathepsin S inhibitor, LY3000328, in healthy subjects: PK/PD and safety and tolerability of cathepsin S inhibitor. *Br. J. Clin. Pharmacol.* **78**, 1334–1342 (2014).
34. Kramer, L., Turk, D. & Turk, B. The future of cysteine cathepsins in disease management. *Trends Pharmacol. Sci.* **38**, 873–898 (2017).
35. Gauthier, J. Y. et al. The discovery of odanacatib (MK-0822), a selective inhibitor of cathepsin K. *Bioorg. Med. Chem. Lett.* **18**, 923–928 (2008).
36. Stoch, S. A. et al. Effect of the cathepsin K inhibitor odanacatib on bone resorption biomarkers in healthy postmenopausal women: two double-blind, randomized, placebo-controlled phase I studies. *Clin. Pharmacol. Ther.* **86**, 175–182 (2009).
37. Bone, H. G. et al. Odanacatib, a cathepsin-K inhibitor for osteoporosis: a two-year study in postmenopausal women with low bone density. *J. Bone Miner. Res.* **25**, 937–947 (2010).
38. Lindström, E. et al. Nonclinical and clinical pharmacological characterization of the potent and selective cathepsin K inhibitor MIV-711. *J. Transl. Med.* **16**, 125 (2018).

39. Hargreaves, P. et al. Differential effects of specific cathepsin S inhibition in biocompartments from patients with primary Sjögren syndrome. *Arthritis Res. Ther.* **21**, 175 (2019).
40. Chen, R. et al. Efficacy and safety of odanacatib for osteoporosis treatment: a systematic review and meta-analysis. *Arch. Osteoporos.* **18**, 67 (2023).
41. Bentley, D., Fisher, B. A., Barone, F., Kolb, F. A. & Attley, G.A randomized, double-blind, placebo-controlled, parallel group study on the effects of a cathepsin S inhibitor in primary Sjögren's syndrome. *Rheumatology* **62**, 3644–3653 (2023).
42. Mullard, A. Merck & Co. drops osteoporosis drug odanacatib. *Nat. Rev. Drug Discov.* **15**, 669–669 (2016).
43. Van Dalen, F. J. et al. Application of a highly selective cathepsin S two-step activity-based probe in multicolor bio-orthogonal correlative light-electron microscopy. *Front. Chem.* **8**, 628433 (2021).
44. Bratkovič, T. et al. Affinity selection to papain yields potent peptide inhibitors of cathepsins L, B, H, and K. *Biochem. Biophys. Res. Commun.* **332**, 897–903 (2005).
45. Gobec, S. & Frlan, R. Inhibitors of cathepsin B. *Curr. Med. Chem.* **13**, 2309–2327 (2006).
46. Hamilton, G. S. Antibody–drug conjugates for cancer therapy: the technological and regulatory challenges of developing drug–biologic hybrids. *Biologicals* **43**, 318–332 (2015).
47. Mullard, A. Maturing antibody–drug conjugate pipeline hits 30. *Nat. Rev. Drug Discov.* **12**, 329–332 (2013).
48. Flygare, J. A., Pillow, T. H. & Aristoff, P. Antibody–drug conjugates for the treatment of cancer. *Chem. Biol. Drug Des.* **81**, 113–121 (2013).
49. Chalouni, C. & Doll, S. Fate of antibody–drug conjugates in cancer cells. *J. Exp. Clin. Cancer Res.* **37**, 20 (2018).
50. Pauly, T. A. et al. Specificity determinants of human cathepsin S revealed by crystal structures of complexes. *Biochemistry* **42**, 3203–3213 (2003).
51. Zoete, V. et al. Attracting cavities for docking. Replacing the rough energy landscape of the protein by a smooth attracting landscape. *J. Comput. Chem.* **37**, 437–447 (2016).
52. Gaieb, Z. et al. D3R Grand Challenge 3: blind prediction of protein–ligand poses and affinity rankings. *J. Comput. Aided Mol. Des.* **33**, 1–18 (2019).
53. Craik, D. J., Fairlie, D. P., Liras, S. & Price, D. The future of peptide-based drugs: peptides in drug development. *Chem. Biol. Drug Des.* **81**, 136–147 (2013).
54. Diao, L. & Meibohm, B. Pharmacokinetics and pharmacokinetic–pharmacodynamic correlations of therapeutic peptides. *Clin. Pharmacokinet.* **52**, 855–868 (2013).
55. Fosgerau, K. & Hoffmann, T. Peptide therapeutics: current status and future directions. *Drug Discov. Today* **20**, 122–128 (2015).
56. Verdoes, M. et al. Improved quenched fluorescent probe for imaging of cysteine cathepsin activity. *J. Am. Chem. Soc.* **135**, 14726–14730 (2013).
57. Edgington-Mitchell, L. E., Bogyo, M. & Verdoes, M. in *Activity-Based Proteomics* (eds Overkleeft, H. S. & Florea, B. I.) vol. 1491 145–159 (Springer, 2017).
58. Segal, E. et al. Detection of intestinal cancer by local, topical application of a quenched fluorescence probe for cysteine cathepsins. *Chem. Biol.* **22**, 148–158 (2015).
59. Barrett, A. J., Kembhavi, A. A. & Hanada, K. E-64 [L-*trans*-epoxysuccinyl-leucyl-amido(4-guanidino)butane] and related epoxides as inhibitors of cysteine proteinases. *Acta Biol. Med. Ger.* **40**, 1513–1517 (1981).
60. Woo, J. T. et al. Suppressive effect of *N*-(benzyloxycarbonyl)-L-phenylalanyl-L-tyrosinal on bone resorption in vitro and in vivo. *Eur. J. Pharmacol.* **300**, 131–135 (1996).
61. Belkhiri, A. et al. Expression of t-DARPP mediates trastuzumab resistance in breast cancer cells. *Clin. Cancer Res.* **14**, 4564–4571 (2008).
62. Egle, A., Harris, A. W., Bath, M. L., O'Reilly, L. & Cory, S. VavP-*Bcl2* transgenic mice develop follicular lymphoma preceded by germinal center hyperplasia. *Blood* **103**, 2276–2283 (2004).
63. Boike, L., Henning, N. J. & Nomura, D. K. Advances in covalent drug discovery. *Nat. Rev. Drug Discov.* **21**, 881–898 (2022).
64. Narayanan, A., Toner, S. A. & Jose, J. Structure-based inhibitor design and repurposing clinical drugs to target SARS-CoV-2 proteases. *Biochem. Soc. Trans.* **50**, 151–165 (2022).
65. López-Otín, C. & Bond, J. S. Proteases: multifunctional enzymes in life and disease. *J. Biol. Chem.* **283**, 30433–30437 (2008).

[1]Swiss Institute for Experimental Cancer Research (ISREC), School of Life Sciences, Swiss Federal Institute of Technology Lausanne (EPFL), Lausanne, Switzerland. [2]Swiss Cancer Center Leman (SCCL), Lausanne, Switzerland. [3]Institute of Chemical Sciences and Engineering (ISIC), Institute of Bioengineering, Swiss Federal Institute of Technology Lausanne (EPFL), Lausanne, Switzerland. [4]Laboratory of Protein Design and Immunoengineering, School of Engineering, Swiss Federal Institute of Technology Lausanne (EPFL), Lausanne, Switzerland. [5]Ludwig Institute for Cancer Research, Lausanne Branch, Lausanne, Switzerland. [6]Department of Oncology, Lausanne University Hospital (CHUV) and University of Lausanne (UNIL), Lausanne, Switzerland. [7]Department of Medical Biosciences, Radboud University Medical Center, Nijmegen, The Netherlands. [8]Institute for Chemical Immunology, Nijmegen, The Netherlands. [9]Translational Radiopharmaceutical Sciences, Departments of Nuclear Medicine and Molecular Imaging and of Oncology, Lausanne University Hospital (CHUV) and University of Lausanne (UNIL), Lausanne, Switzerland. [10]In Vivo Imaging Facility, Department of Research and Training, University of Lausanne (UNIL), Lausanne, Switzerland. [11]Protein Production and Structure Core Facility, School of Life Sciences, Swiss Federal Institute of Technology Lausanne (EPFL), Lausanne, Switzerland. [12]AGORA Pôle de Recherche sur le Cancer, Lausanne, Switzerland. ✉e-mail: bruno.correia@epfl.ch; elisa.oricchio@epfl.ch

Methods

NNPI synthesis

4-Aminocrotonic acid was used for the NNPI synthesis to insert a Michael acceptor in the backbone of the peptidic compound. 4-Aminobutyric acid was used to synthesize the modified version of the NNPI with a single bond replacing the double bond in the Michael acceptor (NNPI-C10-NC). The synthesis of the NNPI libraries for the site saturation mutagenesis screenings was outsourced to GL Biochem. The list of all NNPI sequences synthesized as part of these two libraries is provided together with the Source Data files linked to this article.

Site saturation mutagenesis screenings

A library of 126 NNPIs was screened by FRET assay on CTSS WT, CTSS Y132D and CTSB using 384-well plates. For each of the seven amino acid positions in the original NNPI-3 structure, 18 different amino acid substitutions were tested (we excluded cysteine because it would generate unstable NNPIs that would react with each other in solution and we also excluded the amino acid that was originally present in the NNPI-3 at that position). For the second screening on CTSK and CTSL, another library of 32 NNPIs was used. For each of the amino acids at positions 2 to 7 in the original NNPI-E15 structure, six different amino acid substitutions were tested (A, L, T, W, E or R). The final concentrations of enzyme and substrate were the same as those described in the Supplementary Methods for the respective FRET assays. The final reaction volume per well was 20 µl. The inhibitor concentration was 15 µM for the screenings on CTSS WT and CTSS Y132D, 7.5 µM for CTSB and 30 nM for CTSK and CTSL. Fluorescence emission was measured with a BioTek Neo HTS plate reader. Plate layout, raw data and analyzed data for all five screenings are provided in the Source Data file associated with Fig. 1.

Antibody conjugation

The antibody in PBS buffer at pH 7–7.5 was moved to a 1.5-ml tube or a 15-ml conical centrifuge tube and degassed. The antibody was kept at a concentration of 1–10 mg ml^{-1}. A 30× molar excess of TCEP reagent was added to reduce disulfide bonds; then, the solution was flushed with inert gas (N_2) and incubated for 20 min at room temperature. Next, a 20× molar excess of DBCO-maleimide (Sigma-Aldrich, cat. no. 760668-5MG) was added to the antibody solution, which was then flushed again with inert gas and incubated for 90 min at room temperature with slow rotation. The excess of DBCO-maleimide was then removed using a disposable PD-10 desalting column (Cytiva, cat. no. 17-0851-01). The antibody concentration in the eluted fractions was quantified by Nanodrop. The antibody–DBCO was then conjugated with a 4–10× molar excess (depending on the application) of the azide-NNPI (custom-produced by GL Biochem) or AF488 (Thermo Fisher, cat. no. A10266) at 4 °C overnight. When the application required it, the excess of NNPI or dye was removed using a disposable PD-10 desalting column. The conjugated antibody was stored at 4 °C.

Imaging of gel fluorescence after cathepsin binding assay

After activating CTSS as described in the Supplementary Methods, by diluting it in activation buffer to a concentration of 75 µg ml^{-1} (2 µM), the enzyme was incubated with a 50× molar excess of labeled NNPI-C10–AF488. As a negative control, CTSS was incubated alone, while, in a second control, it was preincubated with 400 µM E64 for 10 min before adding NNPI-C10–AF488. After the addition of loading buffer, all samples were heated for 5 min at 95 °C and run on an SDS–PAGE gel (15%). The gel was imaged with a Typhoon imager (GE Healthcare). Protein loading was later confirmed by Coomassie blue staining (PanReac AppliChem, C.I. 42660).

Mass photometry analysis

Mass photometry is a noninvasive and nondestructive technique for the analysis of molecular masses in solution. This technique is based on interferometric scattering microscopy of single molecules in close proximity of an interface, where interferometric contrast has been shown to be linearly proportional to molecular mass within a range of 40–4,000 kDa (ref. 66). It can be used to measure the molecular mass of single biomolecules and molecular complexes[67–69].

Antibodies and APICs were analyzed alone or after 1-h preincubation with a 10× molar excess of CTSS (previously activated as described in the Supplementary Methods). For each acquisition, 2 µl of antibody or APIC at 100 nM was diluted in 18 µl of 50 mM sodium acetate, 5 mM DTT and 250 mM NaCl, directly on the instrument, a Refeyn TwoMP photometer (Refeyn). Following autofocus stabilization, movies of 120-s duration were recorded. Data acquisition was conducted using AcquireMP software (Refeyn, version 1.2.3) and processed and analyzed with Discover MP software (Refeyn, version 1.2.3).

Cell culture

Human WSU-DLCL2 (obtained from the Leibniz Institute DSMZ repository), Raji (obtained from the American Type Culture Collection (ATCC)), BT-474 (ATCC), Karpas-422 (ATCC), HCC-1569 (ATCC) and SU-DHL-4 (ATCC) cell lines were cultured in RPMI 1640 GlutaMAX medium (Thermo Fisher, cat. no. 1870010) supplemented with 10% FBS (Thermo Fisher, cat. no. 10270-106) and 1% penicillin–streptomycin (Thermo Fisher, cat. no. 15140122). The human RT-4 cell line (ATCC) was cultured in DMEM (Thermo Fisher, cat. no. 41966-029) supplemented with 10% FBS and 1% penicillin–streptomycin. The human PC-3 cell line (ATCC) was cultured in F-12K Nut Mix medium (Thermo Fisher, cat. no. 21127-022) supplemented with 10% FBS and 1% penicillin–streptomycin. HEK293E cells were originally obtained from Life Technologies (Invitrogen) and maintained in EX-CELL 293 serum-free medium from Sigma-Aldrich. ExpiCHO cells were obtained as part of the ExpiCHO Expression System from Thermo Fisher (cat. no. A29133). The A20 mouse diffuse large B cell lymphoma cell line (ATCC, cat. no. ATCC-TIB208, BALB/c background) and the genetic variants generated from it were cultured in RPMI 1640 medium (Thermo Fisher, cat. no. 1870010) supplemented with 10% heat-inactivated FBS, 1 mM sodium pyruvate (Sigma-Aldrich, cat. no. S8636), 2 mM L-glutamine (Thermo Fisher, cat. no. M11-006), 10 mM HEPES (Sigma-Aldrich, cat. no. H3537), 25 µg ml^{-1} gentamicin (Thermo Fisher, cat. no. G1397), 50 mM 2-mercaptoethanol (Thermo Fisher, cat. no. 31350-010) and 5 mM D-glucose (Sigma-Aldrich, cat. no. G8769). The A20-HA-GFP cell line expressing the hemagglutinin (*HA*) gene from influenza virus strain A/Puerto Rico/8/1934 H1N1 (UniProt P03452) was kindly provided by NovImmune SA. All cell lines were authenticated within the past year by short tandem repeat DNA profiling. All cells were maintained at 37 °C in a water-jacketed incubator containing 5% CO_2.

Primary cell isolation and culture

Primary human B cells. Primary human B cells were isolated from peripheral blood mononuclear cells (PBMCs) of healthy donors using the EasySep Human CD19 Positive Selection Kit II (Stemcell Technologies, cat. no. 17854) and EasySep magnet according to the manufacturer's protocol. Cell culture was conducted using R8 medium (RPMI 1640 with 8% human serum (BioWest, cat. no. S4200), 1% GlutaMAX Supplement, 1% penicillin–streptomycin, 1% HEPES, 1% sodium pyruvate, 1% MEM nonessential amino acids and 50 µM 2-mercaptoethanol (all from Gibco, Thermo Fisher)), supplemented with recombinant human IL-4 (40 ng ml^{-1}) (Miltenyi Biotec, cat. no. 130-093-924). Human B cells were cultured at a density of 10^6 cells per ml in six-well plates that were preseeded overnight with the CD154-expressing pulmonary epithelial cell line L2 (gift from J. Di Domizio; 3×10^5 cells per well, irradiated with 40 Gy using the RS 2000 X-ray Biological Irradiator from Rad Source Technologies)[70] at 37 °C, 5% CO_2 in a humidified atmosphere. Proliferating B cells were harvested every 3–4 days, resuspended in fresh R8 medium and transferred to new six-well plates seeded with

fresh irradiated CD154-expressing cells. After 15 days of culture, activated primary human B cells were collected, washed with PBS (1×) and resuspended in R8 medium at a density of 2×10^6 cells per ml for downstream applications.

Osteoclast differentiation. PBMCs were isolated from a healthy donor's buffy coat by density centrifugation using Ficoll-Paque medium (Cytiva, cat. no. 17-1440-02) and PBS.

The isolated PBMCs were cultured in a cell culture flask in RPMI 1640 medium (Thermo Fisher, cat. no. 1870010) supplemented with 10% heat-inactivated FBS, 2 mM L-glutamine (Thermo Fisher, cat. no. M11-006), 1 mM sodium pyruvate (Sigma-Aldrich, cat. no. S8636), 10 mM HEPES (Sigma-Aldrich, cat. no. H3537), 5 mM D-glucose (Sigma-Aldrich, cat. no. G8769), 25 µg ml^{-1} gentamicin (Thermo Fisher, cat. no. G1397), 50 mM 2-mercaptoethanol (Thermo Fisher, cat. no. 31350-010) and 50 ng ml^{-1} macrophage colony-stimulating factor (M-CSF; Thermo Fisher, cat. no. PHC9504). After 72 h, when the attached cells reached confluency, the monolayer was washed with PBS and the adherent M-CSF-dependent macrophages were retrieved from the culture flask. The cells were then resuspended in culture medium, counted and seeded in a 48-well plate at 3×10^4 cells per well in 300 µl of culture medium supplemented with 50 ng ml^{-1} M-CSF. On the following day, the medium was replaced with culture medium supplemented with 50 ng ml^{-1} M-CSF and 60 ng ml^{-1} receptor activator of nuclear factor κB ligand (RANKL; MedChemExpress, cat. no. HY-P73386). Half of the medium was changed after 48 h. Osteoclasts were retrieved after 96 h and used for downstream applications.

Flow cytometry

Receptor expression. To assess receptor expression in multiple tumor cell lines, 2×10^5 cells per condition were washed in FC buffer (PBS (Gibco, Thermo Fisher, cat. no. 10010-015) and 2% BSA (Sigma-Aldrich, cat. no. A7906)) and incubated with 50 µl of human Fc block (BD Biosciences, cat. no. 564219, diluted 1:50) for 15 min. Cells were subsequently stained with FITC-conjugated mouse anti-human CD22 (clone HIB22, BioLegend, cat. no. 302504, diluted 1:200) or AF488-conjugated mouse anti-human HER2 (Clone 24D2, BioLegend, cat. no. 324410, diluted 1:200) antibody for 45 min at 4 °C in FC buffer. Cells were then washed three times to remove unbound antibody, resuspended in PBS and analyzed using an LSR Fortessa FC instrument (BD Biosciences).

Antibody–Dye conjugate internalization. To assess the internalization of antibody–dye conjugates by tumor cell lines, 2×10^5 cells per condition were washed in FC buffer and incubated with 50 µl of human Fc block for 15 min. Cells were subsequently incubated with the antibody–dye conjugate or control compound for 4 h at 4 °C or 37 °C in FC buffer. Next, cells were washed three times to remove unbound antibody and resuspended in PBS; the quencher anti-AF488 antibody (Thermo Fisher, cat. no. A11094) was added to the conditions needing to be quenched and then cells were analyzed using an LSR Fortessa FC instrument (BD Biosciences).

APIC lysosomal delivery. To assess APIC lysosomal delivery, the corresponding APIC was labeled with the pHrodo iFL Red Microscale Protein Labeling kit (Thermo Fisher, cat. no. P36014), following the manufacturer's instructions. A total of 2×10^5 cells per condition were subsequently incubated with the labeled APIC for 150 min at 4 °C or 37 °C. Next, cells were washed three times to remove unbound antibody, resuspended in PBS and analyzed using an LSR Fortessa FC instrument (BD Biosciences).

Cytosolic CD74 accumulation. To assess cytosolic CD74 accumulation in multiple tumor cell lines, 2×10^5 cells per condition were treated in duplicate with the compounds indicated for 24–48 h. At the end of the treatment, the cells were fixed, permeabilized and washed with a Fixation/Permeabilization Kit (BD Biosciences, cat. no. 554714). Cells were then incubated with 50 µl of Fc block (BD Biosciences, cat. no. 564219 for human Fc block and cat. no. 553142 for mouse Fc block, diluted 1:50) for 15 min and subsequently stained with PE-conjugated mouse anti-human CD74 (clone Pin.1; BioLegend, cat. no. 357604, diluted 1:200) or BV711-conjugated rat anti-mouse CD74 (Clone In-1; BD Biosciences, cat. no. 740748, diluted 1:200) antibody for 30 min at room temperature. Cells were then washed three times to remove unbound antibody, resuspended in PBS and analyzed using an LSR Fortessa FC instrument (BD Biosciences).

Splenocyte analysis. FC analysis of spleens isolated from in vivo experiments was performed as previously reported[10]. Briefly, the spleens were smashed and splenocytes were washed in PBS and resuspended in red blood cell lysis buffer (Miltenyi Biotec, cat. no. 130-094-183) for 4 min at room temperature to lyse red blood cells. Then, PBS was added to stop lysis and a 40-µm filter (Falcon, cat. no. 352350) was used to filter the cells and generate a single cell suspension. After cell counting, 2×10^6 cells were incubated for 15 min on ice with 50 µl of Fc block (BD Biosciences, cat. no. 553142, diluted 1:50) in fluorescence-activated cell sorting (FACS) buffer (PBS (Gibco, Thermo Fisher, cat. no. 10010-015) and 2% BSA (Sigma-Aldrich, cat. no. A7906)). Then, samples were supplemented with 50 µl of the following antibody mixture: APC-Cy7-conjugated rat anti-mouse CD45 (clone 30F11; BD Bioscience, cat. no. 557659), PE-CF594-conjugated rat anti-mouse B220 (clone RA3-6B2; BD Bioscience, cat. no. 562313), BV786-conjugated hamster anti-mouse CD3 (clone 145-2C11; BD Bioscience, cat. no. 564379), PerCP-eFluor 710-conjugated rat anti-mouse CD4 (clone RM4-5; Thermo Fisher, cat. no. 46-0042-82) and PE-Cy7-conjugated rat anti-mouse CD8a (clone 53-6.7; BD Bioscience, cat. no. 552877). Samples were subsequently washed three times in FACS buffer, resuspended in 200 µl of FACS buffer containing DAPI viability marker (Molecular Probes, cat. no. D1306) and analyzed using an LSR Fortessa FC instrument (BD Biosciences). The gating strategy used to analyze the FC data is exemplified in Supplementary Fig. 1. In brief, single cells were gated using FSC-H/FSC-A and SSC-H/SSC-A gating; then, live cells were gated using DAPI-negative gating; among live cells, leukocytes were then separated using CD45 gating; among leukocytes, CD3–B220 gating allowed the separation of T cells ($CD3^+$) from B cells ($B220^+$); among $CD3^+$ T cells, CD4–CD8 gating was used to identify $CD4^+$ T cells and $CD8^+$ T cells.

FC data analysis. FC analyses were performed with FlowJo version 10.9.0 software (Tree Star).

Cathepsin labeling in living cells and lysate imaging

The qABPs selective for cysteine cathepsins become fluorescent only after reacting with a cathepsin, which allows an assessment of the enzymatic activity of this class of proteases.

For cellular labeling of cysteine cathepsins, 2×10^5 cells were incubated with the BMV109 probe (200× in DMSO) at 1 µM in culture medium and incubated for 1 h at 37 °C. Where indicated, the cells were preincubated for 6 h with the inhibitory compounds to be tested. For fluorescence SDS–PAGE, the labeled cells were washed with PBS, resuspended in hypotonic lysis buffer (50 mM PIPES pH 7.4, 10 mM KCl, 5 mM $MgCl_2$, 2 mM EDTA, 4 mM DTT and 1% NP-40), put on ice for 15 min and centrifuged at 4 °C, 21,130*g* for 15 min; the supernatants were collected. Equivalent amounts of total protein were denatured by addition of 4× sample buffer (40% glycerol, Tris–HCl (0.2 M, pH 6.8), 8% SDS, 10% β-mercaptoethanol and 0.04% bromophenol blue) and heated for 5 min at 95 °C, before being resolved by SDS–PAGE (15%), and labeled cathepsins were visualized by scanning the gel with a Typhoon imager (GE Healthcare). Protein loading was confirmed by Coomassie blue staining (PanReac AppliChem, C.I. 42660).

The concentrations of tested drugs were as follows:

- Raji cells and primary B cells from healthy donors were treated with anti-CD79 antibody at 3.3 µM, anti-CD79–C10 APIC at 3.3 µM or petesicatib at 40 µM.
- HCC-1569 and RT-4 cells were treated with anti-HER2 antibody at 3.3 µM, anti-HER2–D5 APIC at 3.3 µM or E64 at 40 µM.
- Osteoclasts were treated with NNPI-F17 at 20 µM, anti-SIGLEC-15 antibody at 3.3 µM, anti-SIGLEC-15–F17 APIC at 3.3 µM or odanacatib at 40 µM.
- PC-3 cells were treated with NNPI-G14 at 12 µM, anti-SIGLEC-15 antibody at 2 µM, anti-SIGLEC-15–G14 APIC at 2 µM or Z-FY-CHO at 20 µM.

Mouse models

CL4 TCR transgenic mice were provided by R. Liblau. VavP-*Bcl2* mice were obtained from S. Cory. VavP-*Bcl2 CTSS* KO mice were derived by our laboratory for a previous study[10]. All transgenic animals were maintained in the Swiss Federal Institute of Technology Lausanne (EPFL) animal facilities and all mice were kept in a 12-h light 12-h dark cycle, at 18–23 °C with 40–60% ambient humidity, in accordance with and as recommended by the regulations of the Animal Welfare Act (SR 455) and Animal Welfare Ordinance (SR 455.1). All animal experiments were performed in accordance with the Swiss Federal Veterinary Office guidelines and as authorized by the Cantonal Veterinary Office (animal licenses VD2932.1, VD2993, VD3631 and VD3701).

Randomization

VavP-*Bcl2* mice were randomized in the treatment groups without any knowledge about tumor development. They were allocated randomly to the treatment groups, ensuring that mice of comparable age were assigned to each group. For the imaging of CTSS enzymatic activity in vivo, as well as for the biodistribution experiments, allocation to treatment groups was not random but based on tumor volume, to have mice with similar tumor volumes in each group. No special randomization criterion was needed for our molecular, biochemical and cellular experiments.

Sample size

For VavP-*Bcl2* mice, the estimated effect size for the difference in the number of B cells in the spleen of animals is large when comparing WT and genetically modified *CTSS* KO mice[10], which meant that a sample size of three mice per group could be enough to observe a significant difference in such a case. Even though we aimed to obtain the same phenotype, the experimental setup was different and, thus, the sample size had to be greater. Because we planned to treat the mice with an inhibitor for a limited time frame and pharmacological inhibitors rarely achieve complete inhibition, we decided to perform the experiment with five mice per treatment group.

For the imaging of CTSS enzymatic activity, we did not find examples of in vivo comparisons of cathepsin activity in WT versus cathepsin KO models or upon CTSS inhibitor treatment in the literature; therefore, we could not estimate the effect size a priori. On the basis of similar experiments reported in the literature to study the activity of other cathepsins in vivo using the same molecular probe[56], we decided to use three mice per treatment group.

For the biodistribution experiments, the number of animals was chosen on the basis of what is suggested by the literature and normally used for these standard experiments[71].

Subcutaneous Raji tumors

A total of 2.5×10^6 Raji WT or *CTSS* KO cells were injected subcutaneously into the right flank of 8–10-week-old NSG (NOD.Cg-*Prkdc*^{scid} *Il2rg*^{tm1Wjl}/SzJ) mice under isoflurane anesthesia. The maximal tumor size permitted by the corresponding animal license (as listed above) is 1,000 mm^3. Tumors were measured every 2–3 days using a caliper and volumes were calculated using the formula $(\text{width} \times \text{length} \times \text{height} \times \pi)/6$. Animals were killed right before the tumor volume reached 1,000 mm^3 or at the experimental endpoint.

In vivo treatment and imaging of cathepsin activity

To evaluate cathepsin inhibition by the anti-CD79–C10 APIC in vivo, treatment was started when tumors reached a diameter of ≥5 mm in all animals. Mice were treated intraperitoneally with either 500 µg of anti-CD79–C10 APIC or 500 µg of anti-CD79 antibody twice, with the second injection 24 h after the first. Then, 48 h after the first injection, the BMV109 probe (20 nmol; 0.8 nmol g^{-1}) was administered through the tail vein in a volume of 100 µl (20% DMSO in PBS). Next, 8 h after injection, mice were imaged noninvasively using a Xenogen IVIS Imaging System 200 (PerkinElmer). The images were analyzed with Living Image software (PerkinElmer, version 4.8.0). Gates of the same size were used to measure the signal radiating from the tumor for all seven mice.

Treatment of VavP-*Bcl2* mice

To assess the efficacy of APIC treatment, VavP-*Bcl2* female mice were treated intraperitoneally twice a week for a total of five times over 17 days with anti-mouse CD79–C10 APIC or unconjugated anti-mouse CD79 antibody (20 mg kg^{-1} dose; five mice per group, age-matched and 21–30 weeks old at treatment start). Then, 3 days after the last injection, mice were killed and the spleen was collected for FC and histology analyses. One VavP-*Bcl2 CTSS* KO mouse of the same age was killed on the same day to collect its spleen for analysis.

Multiplexed immunofluorescence analysis

The 4plex immunofluorescence was performed as previously described[10], using the fully automated Ventana Discovery ULTRA (Roche Diagnostics) with Ventana solutions, following the manufacturer's recommendations. Briefly, dewaxed and rehydrated paraffin sections were pretreated with heat using standard condition (40 min) CC1 solution. The primary antibodies used were as follows: rat anti-mouse F4/80 (clone Cl:A3-1; Bio-Rad, cat. no. MCA497GA), rat anti-mouse CD8 (clone 4SM15; eBioscience, cat. no. 14-0808-82), rat anti-mouse CD4 (clone 4SM95; eBioscience, cat. no. 14-9766-82) and rat anti-mouse B220 (clone RA3-6B2; eBioscience, cat. no. 13-0452-82), which were applied sequentially and incubated at 37 °C for 1 h. The samples were incubated with rat ImmPRESS HRP (ready to use, VectorLabs) and then the primary antibodies used were revealed with the Rhodamine 6G (Ventana, cat. no. 760-244), Red 610 (Ventana, cat. no. 760-245), Cyanine 5 (Ventana, cat. no. 760-238) and fluorescein amidite (Ventana, cat. no. 760-243) fluorescent kits (Roche Diagnostics), respectively. Between each antibody labeling step, heat denaturation was performed. Slides were subsequently acquired using an Olympus VS120 slide scanner (Evident) and later analyzed using QuPath.

Quantification and statistical analysis

For FRET, FC, transwell invasion, viability and *in vivo* experiments, data were analyzed and plotted using the software GraphPad Prism 9. The results represented in bar plots report the mean ± s.d. of the indicated number of independent replicates. The central line of the box plots indicates the median, the whiskers indicate the maximum and minimum values and the box limits correspond to the 25th and 75th percentiles. Two-tailed *t*-tests, *F*-tests and one-way analyses of variance were used as indicated in the legends. Details on the quantification, normalization and statistical tests used in every experiment can be found in the corresponding figure legends, including the number of independent replicates in each experiment. Data collection and analysis were not performed blind to the conditions of the experiments. Data distribution for the measurements taken in the context of in vivo experiments was assumed to be normal but this was not formally tested

for the present study. No animal was excluded from the analysis of the in vivo experiments.

Reporting summary

Further information on research design is available in the Nature Portfolio Reporting Summary linked to this article.

Data availability

The atomic models related to this study have been deposited to the PDB under accession codes 8PI3 and 8RND. Source data are provided with this paper.

References

66. Young, G. et al. Quantitative mass imaging of single biological macromolecules. *Science* **360**, 423–427 (2018).
67. England, R. M., Moss, J. I., Gunnarsson, A., Parker, J. S. & Ashford, M. B. Synthesis and characterization of dendrimer-based polysarcosine star polymers: well-defined, versatile platforms designed for drug-delivery applications. *Biomacromolecules* **21**, 3332–3341 (2020).
68. Bertosin, E. et al. Cryo-electron microscopy and mass analysis of oligolysine-coated DNA nanostructures. *ACS Nano* **15**, 9391–9403 (2021).
69. Naftaly, A., Izgilov, R., Omari, E. & Benayahu, D. Revealing advanced glycation end products associated structural changes in serum albumin. *ACS Biomater. Sci. Eng.* **7**, 3179–3189 (2021).
70. Garrone, P. et al. Fas ligation induces apoptosis of CD40-activated human B lymphocytes. *J. Exp. Med.* **182**, 1265–1273 (1995).
71. Delage, J. A. et al. Copper-64-labeled 1C1m-Fc, a new tool for TEM-1 PET imaging and prediction of lutetium-177-labeled 1C1m-Fc therapy efficacy and safety. *Cancers* **13**, 5936 (2021).

Acknowledgements

We thank the EPFL and University of Lausanne (UNIL) facilities, particularly the Protein Production and Structure Core Facility, the Biomolecular Screening Facility, the Institute of Chemical Sciences and Engineering (ISIC) Mass Spectrometry Facility and the FC Core Facility of EPFL. We also thank M. Santin, A. Buu-Hoang, E. Simkova, A. Pellegrino and G. Dienes from EPFL for their technical support with in vitro assay optimization. This work was supported by the SNF (Spark grant CRSK-3_190639, to E.O.), Leenaards Foundation (to E.O., B.E.C. and C.A.), Swiss Cancer League (KFS-5000-02-2020, to E.O.) and Fondation Aclon (to E.O.). We thank ARRONAX (Saint Herblain, France) for [^{64}Cu] production. We thank Creoptix (Wädenswil, Switzerland) and A. Moretti for support with the Creoptix WAVE system.

Author contributions

A.P., B.E.C. and E.O. conceptualized the study. A.P. performed all the biochemical and cellular assays and animal experiments. A.P. analyzed and plotted the data. M.B., A.S.-M. and N.K. contributed to the animal experiments. L.R. contributed to non-natural peptide synthesis. S.W. and S.G. helped with antibody cloning and protein production and purification. D.I. contributed to experiments with primary cells. F.J.v.D. performed the synthesis of the qABP. D.V. performed the radiolabeling and biodistribution studies and related data analysis, with help from A.P. K.L. contributed to protein production, purification and crystallography experiments, as well as related data analysis, with help from F.P. V.Z. performed the molecular docking analysis and plotted the corresponding data. E.O., B.E.C., C.A., M.V., M.S. and F.P. supervised the different aspects of the study. E.O., A.P. and B.E.C. wrote the manuscript with comments from all authors.

Competing interests

EPFL has filed two provisional patent applications that incorporate the findings presented in this Article. E.O., A.P. and B.E.C. are named as coinventors on the first patent (European Patent Office, PCT International Application Number PCT/EP2022/073211). E.O. and A.P. are also named as coinventors on the second patent (European Patent Office, Application Number EP24157666.9). The two patent applications cover the structure of the cathepsin inhibitors described in this study. The remaining authors declare no competing interests.

Additional information

Extended data is available for this paper at https://doi.org/10.1038/s41589-024-01627-z.

Supplementary information The online version contains supplementary material available at https://doi.org/10.1038/s41589-024-01627-z.

Correspondence and requests for materials should be addressed to Bruno E. Correia or Elisa Oricchio.

Peer review information *Nature Chemical Biology* thanks Anthony Rullo and the other, anonymous reviewer(s) for their contribution to the peer review of this work.

https://doi.org/10.1038/s41589-024-01627-z

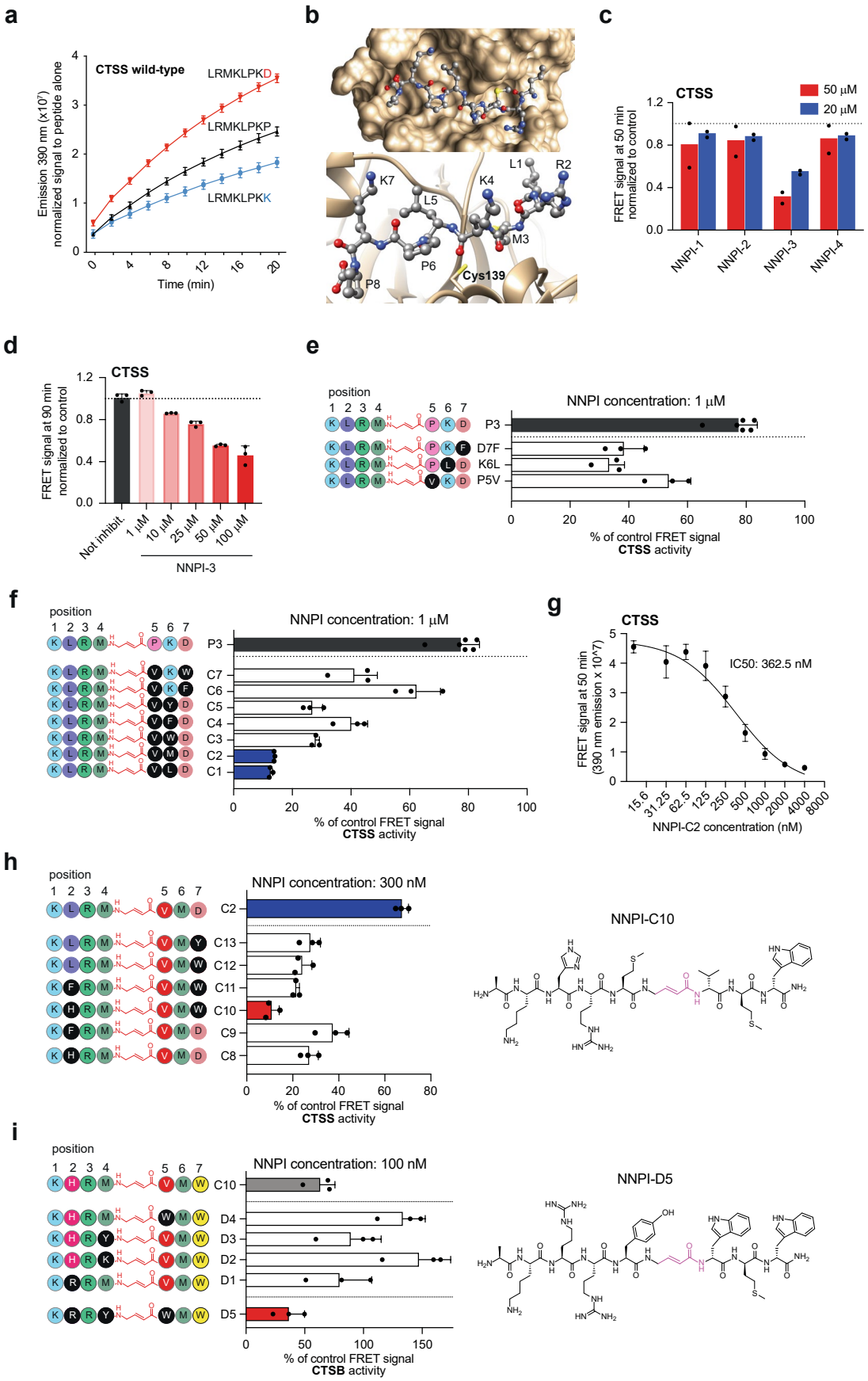

Extended Data Fig. 1 | See next page for caption.

https://doi.org/10.1038/s41589-024-01627-z

Extended Data Fig. 1 | Design and development of NNPIs targeting CTSS or CTSB. a) FRET assay assessing cleavage of 3 different substrate peptides by CTSS (n = 3 independent replicates; mean and SD values are shown). **b**) Binding mode of the CD74 peptide LRMKLPKP calculated using the Attracting Cavities docking software. In the top panel, the CTSS surface is displayed and colored in brown. The peptide is shown in ball and stick representation. The central KL residues of the CD74 peptide are calculated to be in the vicinity of the CTSS Cys139 catalytic residue, labeled in bold (bottom). **c**) Results of FRET assay testing CTSS inhibition by NNPI-1, 2, 3 and 4 (n = 2 independent replicates). **d**) FRET assay assessing CTSS inhibition at increasing NNPI-3 concentrations (n = 3 independent replicates; mean and SD values are shown). **e**) Sequence and CTSS inhibition capacity of different NNPIs with single amino acid substitutions compared to NNPI-3 (n = 3 independent replicates; mean and SD values are shown). **f**) Sequence and CTSS inhibition capacity of different NNPIs combining 2 amino acid substitutions compared to NNPI-3 (n = 3 independent replicates; mean and SD values are shown). The most potent NNPIs are labeled in blue. **g**) FRET dose-response quantification of CTSS inhibition by NNPI-C2 (n = 3 independent replicates; mean and SD values are shown). **h**) Sequence and CTSS inhibition capacity of different NNPIs combining up to 2 new amino acid substitutions compared to NNPI-C2 (n = 3 independent replicates; mean and SD values are shown). The most potent NNPI is labeled in red, and its molecular structure is represented on the right. **i**) Sequence and CTSB inhibition capacity of different NNPIs with up to 3 amino acid substitutions compared to NNPI-C10 (n = 3 independent replicates; mean and SD values are shown). The most potent NNPI is labeled in red, and its molecular structure is represented on the right.

https://doi.org/10.1038/s41589-024-01627-z

a

	conc. of enzyme in assay [nM]	IC50 drug/enzyme molar ratio			
		NNPI-C10	NNPI-D5	NNPI-F17	NNPI-G14
CTSS	13.5	**5.24**	2421.5	42.03	> 148.1
CTSB	11.6	10.1	**5.93**	> 26	13.2
CTSK	0.267	622.5	> 3750	**15.80**	> 1200
CTSL	0.25	778.4	129.2	12.24	**6.68**
CTSH	12.8	> 156.3	> 156.3	> 156.3	> 156.3
CTSZ	6.1	> 163.9	> 163.9	> 163.9	> 163.9
CTSC	4.9	> 204.1	> 204.1	> 204.1	> 204.1

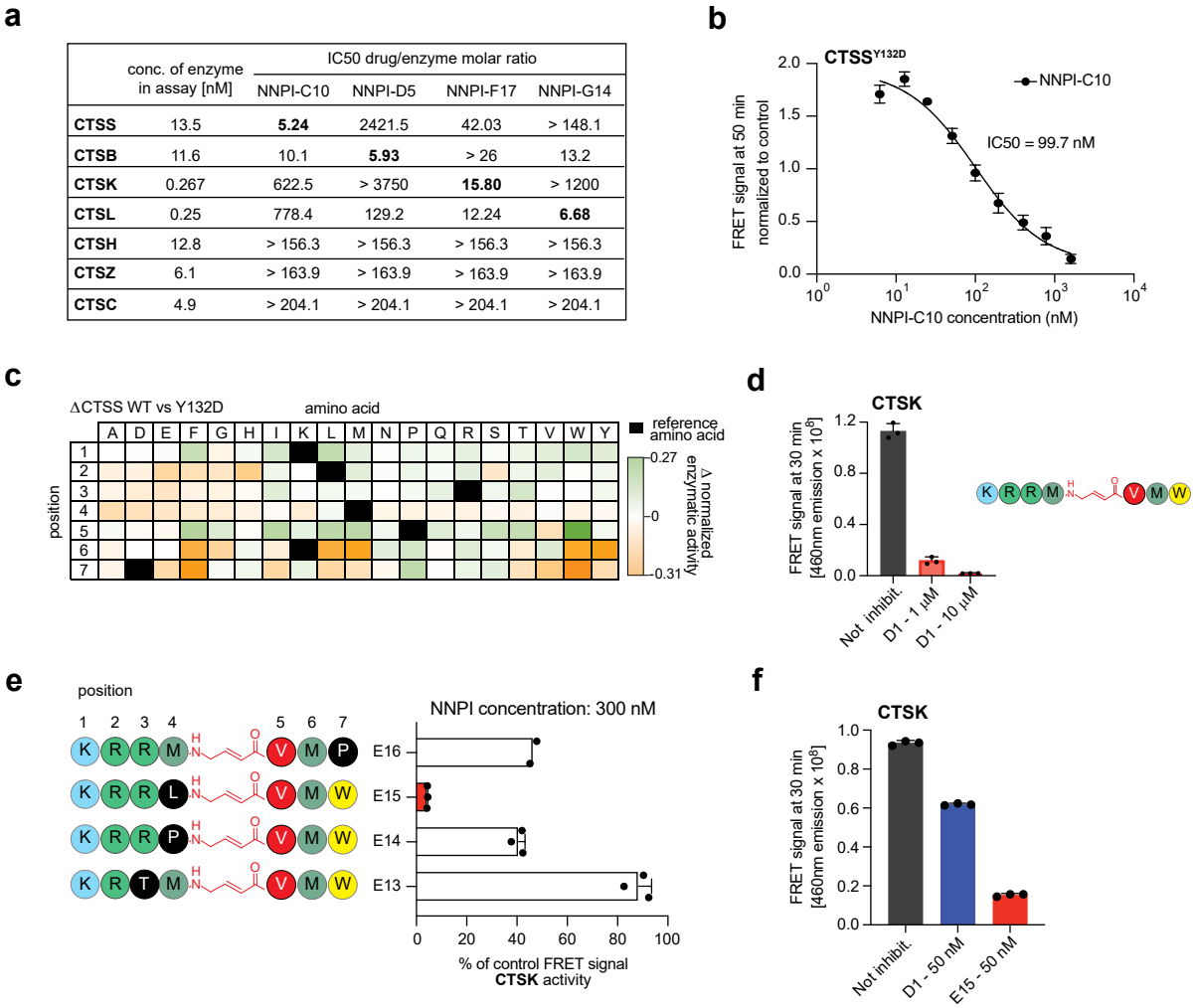

Extended Data Fig. 2 | NNPIs specificity and activity on CTSS Y132D. **a**) IC_{50} values illustrating potency and specificity of NNPI-C10, D5, F17 and G14 based on FRET assays performed on a panel of 7 different cysteine cathepsin proteases (n = 3 for each condition in each FRET assay). IC_{50} values are given as a ratio of drug/enzyme molar concentration in the assay. **b**) Dose-response curve quantifying the inhibitory potency of NNPI-C10 on CTSS Y132D (n = 3 independent replicates; mean and SD values are shown). **c**) Site saturation mutagenesis screening differential results comparing inhibitors on CTSS WT and CTSS Y132D. Amino acid changes colored in green favor inhibition of the mutant form over the wild-type one, whereas the orange ones work better on the wild-type form and less on the mutant CTSS (n = 2 independent replicates). **d**) FRET assay assessing CTSK inhibition at increasing NNPI-D1 concentrations (n = 3 independent replicates; mean and SD values are shown). **e**) Sequence and CTSK inhibition capacity of different NNPIs with single amino acid substitutions compared to NNPI-D1 (n = 3 independent replicates; mean and SD values are shown). The most potent NNPI is labeled in red. **f**) FRET assay assessing CTSK inhibition by NNPI-D1 and NNPI-E15 at 50 nM (n = 3 independent replicates; mean and SD values are shown).

https://doi.org/10.1038/s41589-024-01627-z

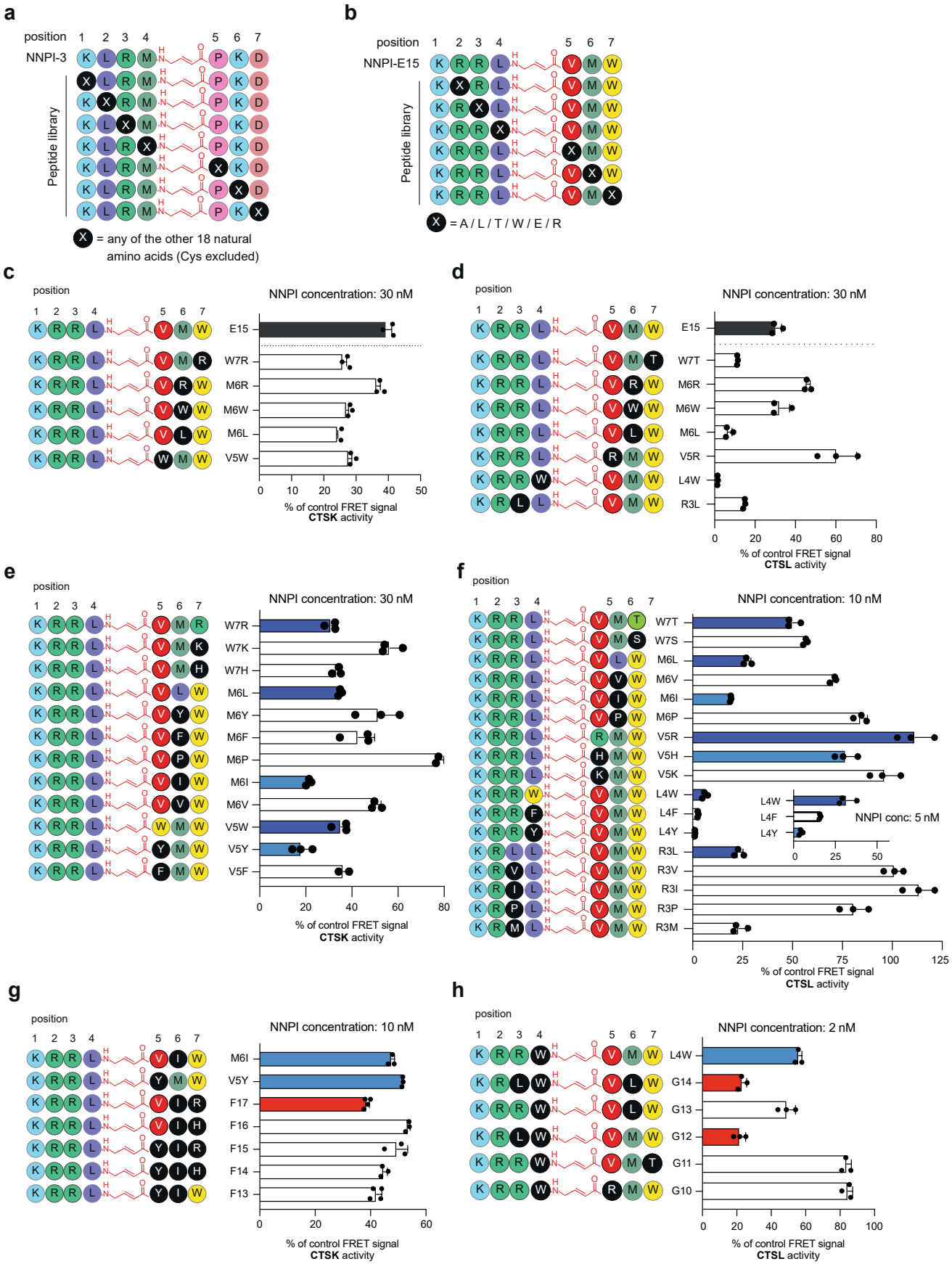

Extended Data Fig. 3 | See next page for caption.

https://doi.org/10.1038/s41589-024-01627-z

Extended Data Fig. 3 | NNPI mutagenesis screening libraries and structural changes to obtain potent CTSK and CTSL inhibitors. a, **b**) Single-site mutagenesis screening libraries applied to CTSS and CTSB (a) or CTSK and CTSL (b). **c**, **d**) Sequence and inhibitory potency of different NNPIs with single amino acid substitutions tested on CTSK (c) or CTSL (d) compared to NNPI-E15 (n = 3 independent replicates; mean and SD values are shown). **e**, **f**) Sequence and inhibitory potency of different NNPIs with alternative single amino acid substitutions tested on CTSK (e) or CTSL (f) compared to the most potent NNPIs identified in the previous screening step (labeled in dark blue). The best NNPIs identified are labeled in light blue (n = 3 independent replicates; mean and SD values are shown). **g**, **h**) Sequence and inhibitory potency of different NNPIs combining up to 3 amino acid changes compared to NNPI-E15 (n = 3 independent replicates; mean and SD values are shown), tested on CTSK (g) or CTSL (h). The most potent NNPIs are labeled in red.

https://doi.org/10.1038/s41589-024-01627-z

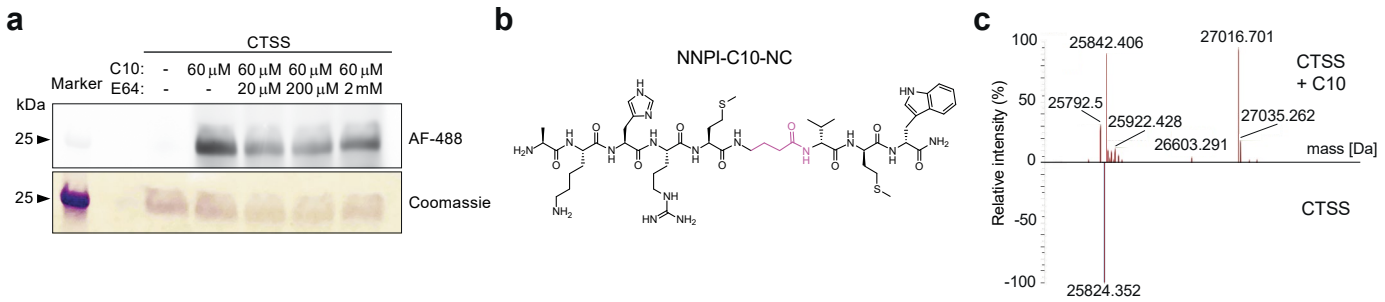

Extended Data Fig. 4 | Assessment of covalent bond formation between NNPI-C10 and CTSS. a) Fluorescence and coomassie blue staining of gel loaded with CTSS alone or incubated with AF488-derivatized NNPI-C10. Different concentrations of E64 were tested to assess if NNPI-C10 could be displaced from CTSS. Images of 1 out of 2 independent experiments represented. **b**) Molecular structure of NNPI-C10-NC, differing from C10 because of a single bond replacing the double bond in the Michael acceptor. **c**) Intact mass spectrometry analysis of CTSS in complex with NNPI-C10 (red peaks) compared to CTSS alone (black peaks), performed in denaturing conditions.

https://doi.org/10.1038/s41589-024-01627-z

a

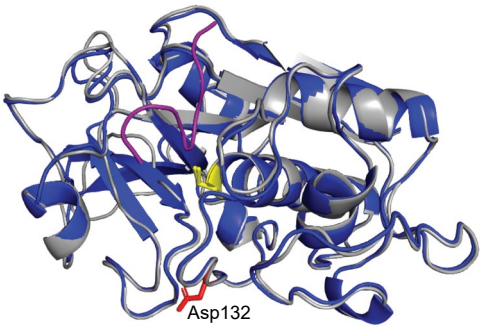

b

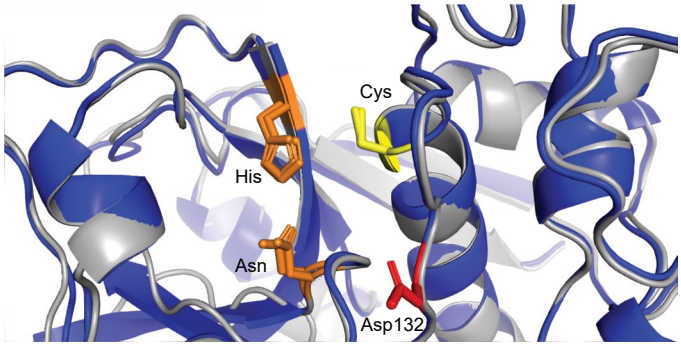

c

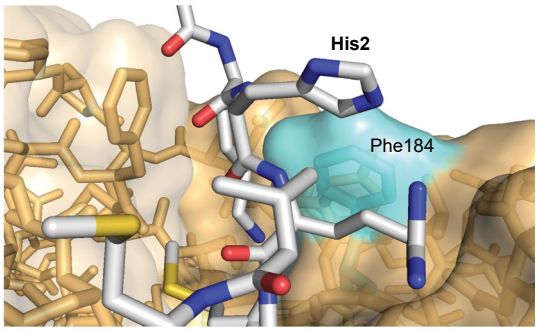

d

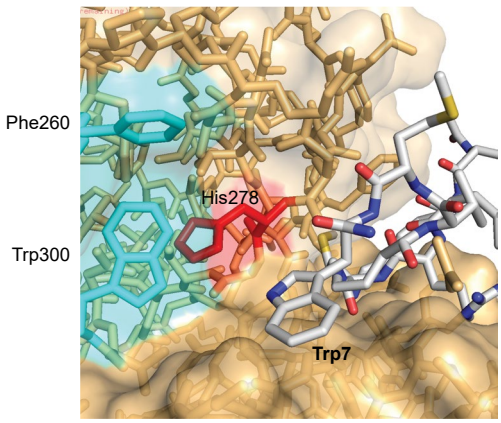

e

CTSS residue	NNPI-C10 residue	Donor atom	Acceptor atom	Distance (nm)
Asn181	Arg3	NE (*C10*)	O	0.22
Asn181	Arg3	NH2 (*C10*)	O	0.22
Gly183	Met4	N (*C10*)	O	0.18
Gly183	Met4	N (*CTSS*)	O	0.21
Asn277	Michael acceptor	N (*C10*)	O	0.21

Extended Data Fig. 5 | Crystal structures of NNPI-C10 in complex with CTSS. a, **b**) Superposed crystal structures of CTSS WT (grey) and CTSS Y132D (blue). Backbone structure of NNPI-C10 represented in purple. Active cysteine represented in yellow, aspartate 132 in red, histidine and asparagine from the catalytic triad in orange. **c**) Proximity of histidine in position 2 of NNPI-C10 and phenylalanine 184 of CTSS (highlighted in light blue). **d**) Position of tryptophan at the C-terminus of NNPI-C10 and phenylalanine 260 and tryptophan 300 of CTSS (highlighted in light blue). Histidine 278 of CTSS is also highlighted in red. **e**) Summary of hydrogen bonds identified between NNPI-C10 and CTSS Y132D.

https://doi.org/10.1038/s41589-024-01627-z

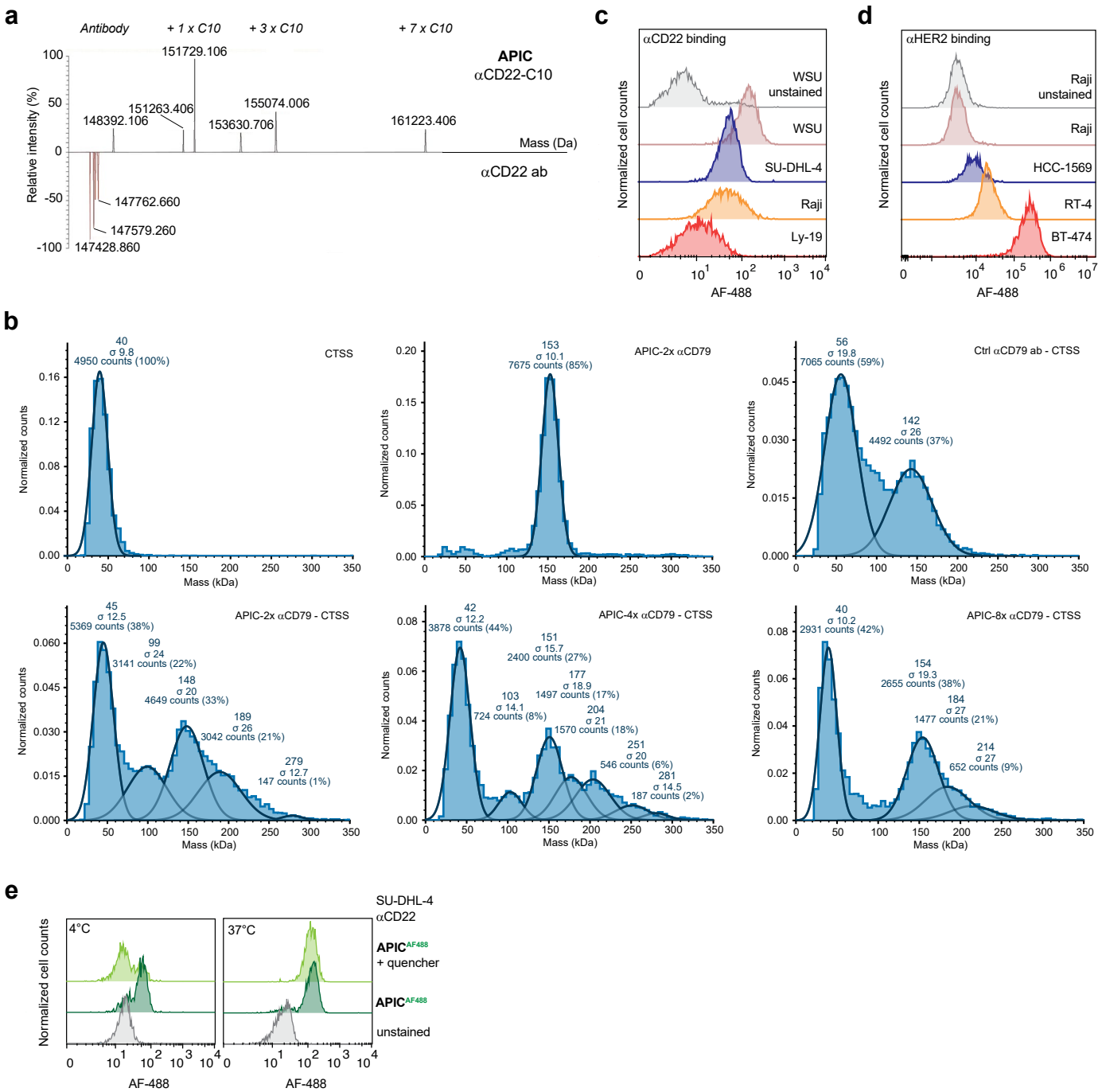

Extended Data Fig. 6 | Antibody-peptide inhibitor conjugates (APIC) characterization. a) Intact mass spectrometry analysis of the αCD22-C10 APIC (black peaks) compared to the unconjugated αCD22 antibody (red peaks). **b**) Mass photometry analyses of CTSS, αCD79 antibody or αCD79-C10 APIC alone or incubated together. APIC conjugated with a 2-fold, 4-fold or 8-fold molar excess of C10-NNPI was used. CTSS was always used in 10-fold molar excess to antibody or APIC. Histograms represented in Fig. 2c were obtained by overlaying data from this experiment. **c**, **d**) Flow cytometry analysis of CD22 (c) and HER2 (d) surface receptor expression in different B cell lymphoma (WSU-DLCL2, SU-DHL-4, Raji, Ly-19), breast cancer (HCC-1569, BT-474) and bladder cancer (RT-4) cell lines. One representative histogram per cell line is shown (n = 2 per cell line). **e**) Flow cytometry analysis of SU-DHL-4 lymphoma cells stained with AF-488 labeled APIC. An anti-AF-488 antibody was used to quench the signal of the fluorophore and assess the internalization of the APIC at 4 °C and 37 °C (n = 2 per condition).

https://doi.org/10.1038/s41589-024-01627-z

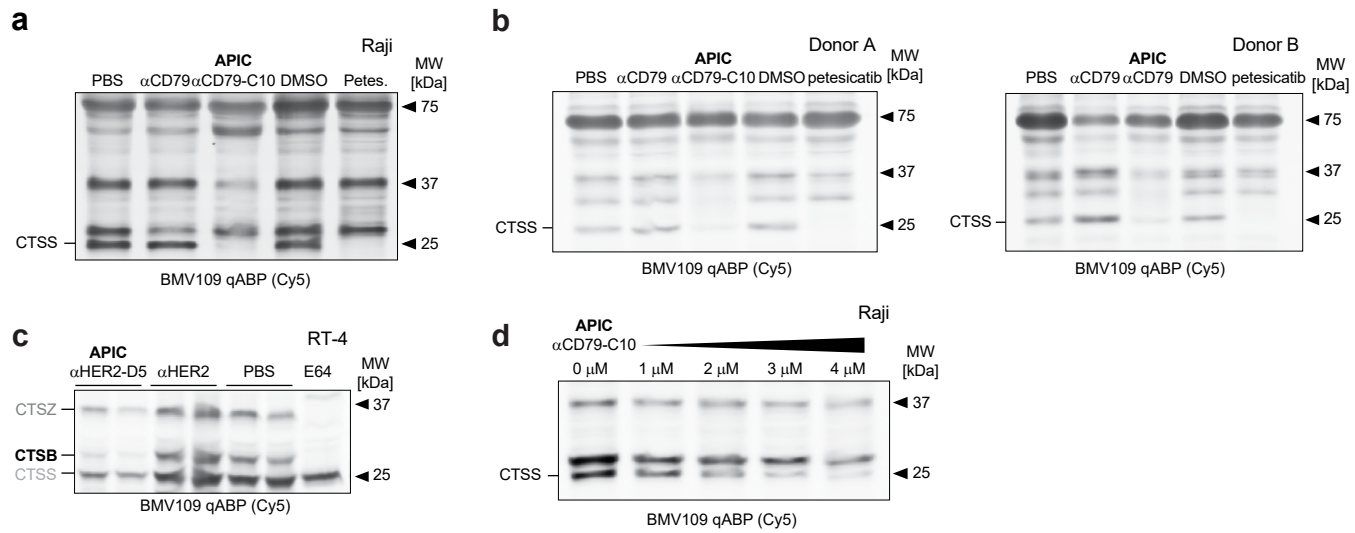

Extended Data Fig. 7 | Cathepsin inhibition by APICs in cellular assays. **a**, **b**) CTSS inhibition in Raji cells (a) or human donor primary B cells (b) treated with αCD79 APIC or petesicatib, assessed by BMV109 quenched activity-based probe (qABP). **c**) CTSB inhibition in RT-4 bladder cancer cells assessed by BMV109 qABP. **d**) Dose-dependent CTSS inhibition in Raji cells treated with increasing concentration of αCD79 APIC assessed by BMV109 quenched activity-based probe (qABP).

https://doi.org/10.1038/s41589-024-01627-z

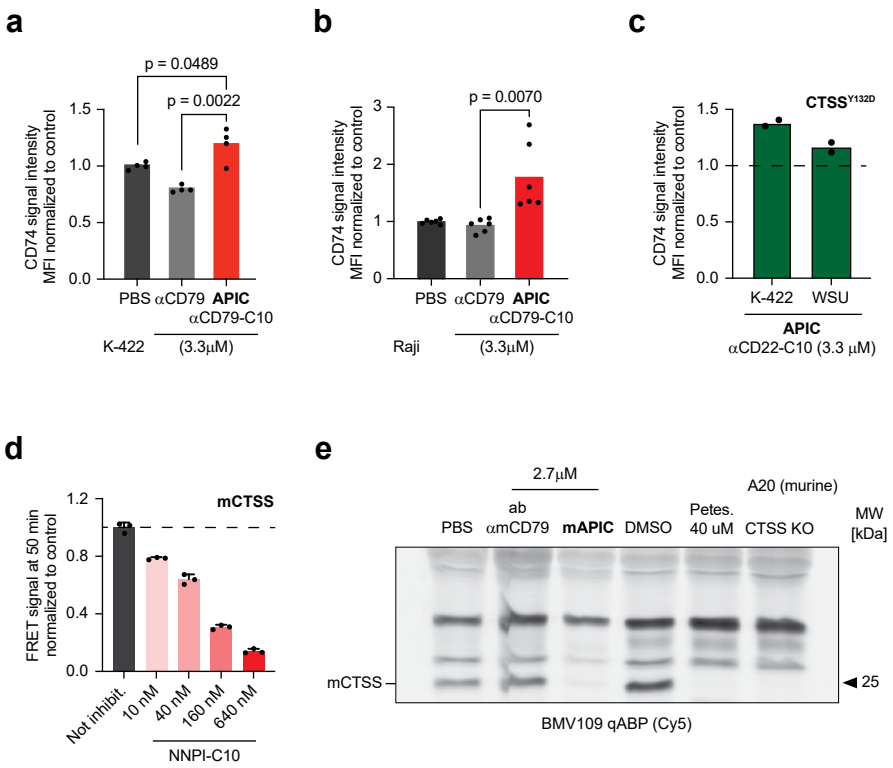

Extended Data Fig. 8 | Functional effects of *in vitro* antibody-peptide inhibitor conjugate treatment of tumor cells. a, **b**) CD74 accumulation measured by flow cytometry in Karpas-422 (a, n = 4 independent wells per condition) and Raji (b, n = 6 independent wells per condition) cells after 48 h incubation with APIC (red), unconjugated antibody (grey) or PBS (black). Median fluorescence intensity (MFI) normalized to PBS condition. P-value was determined by two-tailed t-test. **c**) CD74 accumulation measured by flow cytometry in Karpas-422 and WSU-DLCL2 cells overexpressing CTSS Y132D mutant form, after a 48 h treatment with αCD22 APIC. MFI normalized to signal in control antibody-treated cells (n = 2 independent wells treated per condition). **d**) Quantification of FRET assay assessing murine CTSS inhibition at increasing NNPI-C10 concentrations (n = 3 independent replicates; mean and SD values are shown). **e**) Murine CTSS inhibition in A20 cells treated with αCD79 APIC or petesicatib, assessed by BMV109 qABP. Lysate from untreated CTSS KO A20 cells was loaded as control.

https://doi.org/10.1038/s41589-024-01627-z

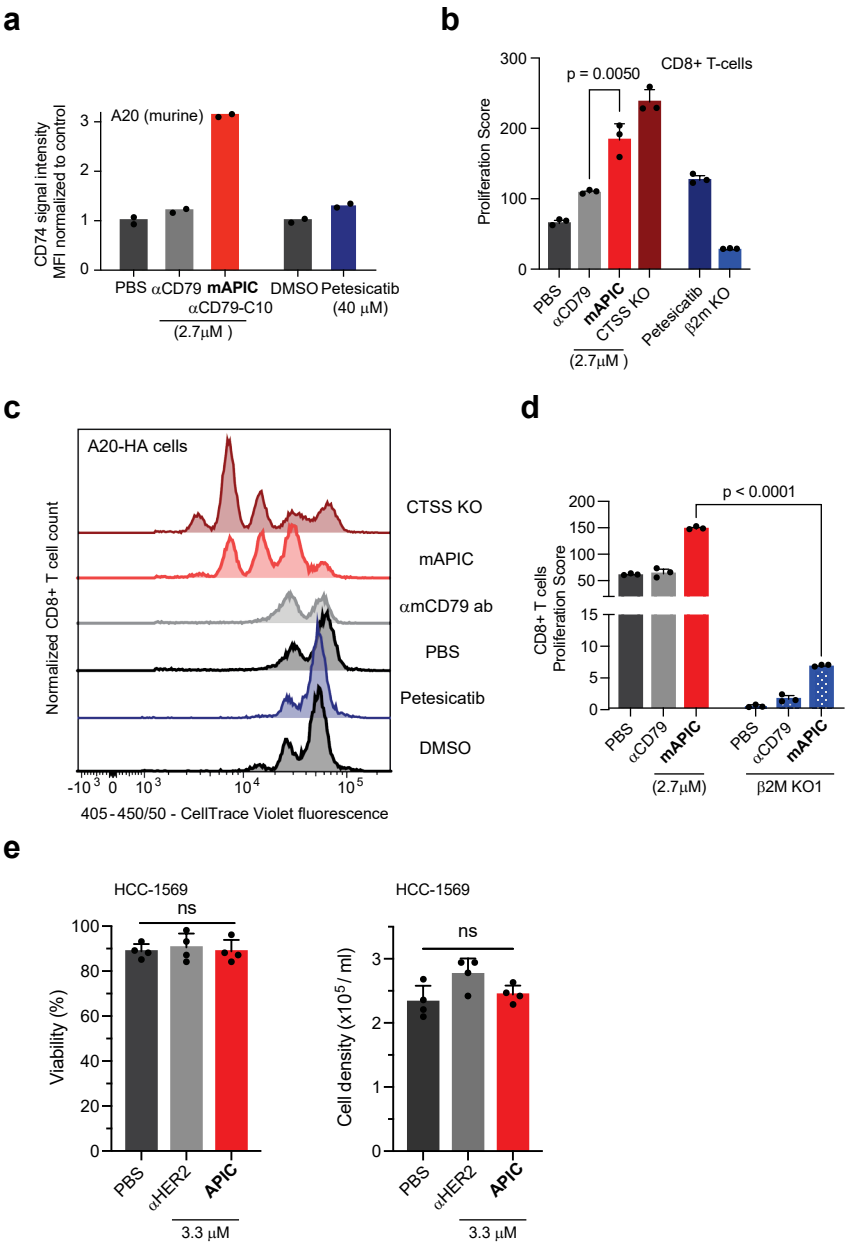

Extended Data Fig. 9 | APIC efficacy in T cell assay and transwell assay. a) CD74 accumulation measured by flow cytometry in A20 cells after 24 h incubation with APIC (red), unconjugated antibody (grey) or PBS (black). Petesicatib (blue) and respective DMSO control (black) were tested in parallel. MFI normalized to PBS condition (n = 2 independent wells treated per condition). **b**, **c**) Proliferation score (b) and representative proliferation peaks (c) of CD8 T cells measured by flow cytometry after 72 hours of co-culture upon treatment with APIC (red), control antibody (grey), PBS (black) or Petesicatib (dark blue). CTSS KO A20 cells (dark red) and B2m KO A20 cells (blue) were included as controls (n = 3 independent wells treated per condition; mean and SD values are shown). P-value was determined by two-tailed t-test. **d**) Comparison of proliferation score of CD8 T cells co-cultured with A20 WT *versus* B2m KO lymphoma cells, measured by flow cytometry after 72 hours of co-culture upon treatment with APIC, control antibody or PBS (n = 3 independent wells treated per condition; mean and SD values are shown). P-value was determined by two-tailed t-test. **e**) Viability and cell density of HCC-1569 breast cancer cells after 48 hour treatment with APIC (red), control antibody (grey) or PBS (black) (n = 3 independent wells treated per condition; mean and SD values are shown). P-values were determined by one-way ANOVA.

https://doi.org/10.1038/s41589-024-01627-z

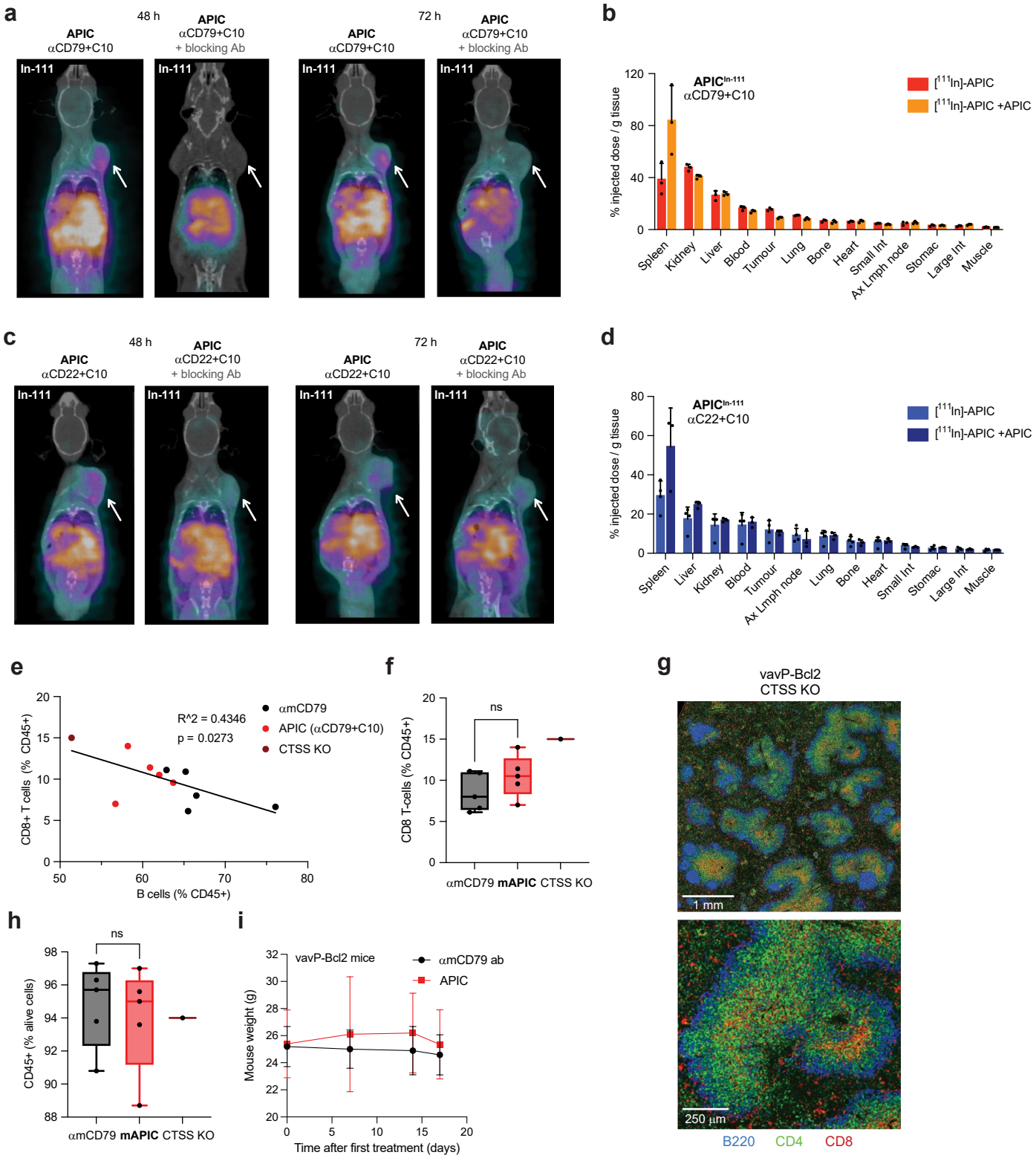

Extended Data Fig. 10 | See next page for caption.

https://doi.org/10.1038/s41589-024-01627-z

Extended Data Fig. 10 | Biodistribution and *in vivo* efficacy of antibody-peptide inhibitor conjugates in human xenograft and syngeneic lymphoma mouse models. a) Fused coronal SPECT/CT images at 48/72 hours post-injection of [^{111}In]NOTA-αCD79 APIC in NSG mice bearing Raji subcutaneous tumors. Tumor mass indicated by a white arrow (n = 2 per condition). **b**) Biodistribution of [^{111}In]NOTA-αCD79 APIC (red, n = 3; mean and SD values shown) in Raji tumor-bearing NSG mice. To demonstrate CD79 specificity of [^{111}In]NOTA-APIC uptake, a 1 mg excess of unlabeled APIC was co-injected (orange, n = 3; mean and SD values shown). **c**) Fused coronal SPECT/CT images at 48/72 hours post-injection of [^{111}In]NOTA-αCD22 APIC in NSG mice bearing Raji tumors (mass indicated by white arrow). **d**) Biodistribution of [^{111}In]NOTA-αCD22 (blue, n = 4; mean and SD values shown) in Raji tumor-bearing mice. To demonstrate specificity, a 1 mg excess of unlabeled APIC was co-injected (dark blue, n = 3). **e**) Negative correlation between the percentage of B cells and CD8+ T cells in the spleen of mice treated with APIC (red, n = 5) or unconjugated anti-mCD79 antibody (black, n = 5) and a CTSS KO control mouse. A straight line was fitted by simple linear regression. P-value was determined by two-tailed F-test. **f**) Flow cytometry quantification of CD8+ T cells in the spleen of mice treated with APIC (red) or anti-mCD79 antibody (gray) (n = 5 mice per group). One age-matched control CTSS KO mouse (dark red) was included as reference. **g**) Representative images of multicolor immunofluorescence of the spleen of a vavP-Bcl2 CTSS KO mouse. Markers: B220 for B cells (blue), CD4 for CD4+ T cells (green), and CD8 for CD8+ T cells (red). A representative region of the larger spleen section stained is shown. **h**) Flow cytometry quantification of CD45+ cells in the spleen of mice treated with APIC (red) or anti-mCD79 antibody (gray) (n = 5 mice per group). One age-matched control CTSS KO mouse (dark red) was included as reference. i) Evolution of body weight of mice treated with APIC (red) or unconjugated anti-mCD79 antibody (black) (n = 5 mice per group; mean and SD values shown). In panels f and h, the central line of boxplots indicates the median value, whiskers indicate the maximum and minimum value; box limits correspond to the 25th-75th percentiles. P-values were determined by two-tailed t-test.

nature portfolio

Corresponding author(s): Elisa Oricchio
Bruno Correia

Last updated by author(s): Mar 5, 2024

Reporting Summary

Nature Portfolio wishes to improve the reproducibility of the work that we publish. This form provides structure for consistency and transparency in reporting. For further information on Nature Portfolio policies, see our Editorial Policies and the Editorial Policy Checklist.

Statistics

For all statistical analyses, confirm that the following items are present in the figure legend, table legend, main text, or Methods section.

n/a	Confirmed
☐	☒ The exact sample size (*n*) for each experimental group/condition, given as a discrete number and unit of measurement
☐	☒ A statement on whether measurements were taken from distinct samples or whether the same sample was measured repeatedly
☐	☒ The statistical test(s) used AND whether they are one- or two-sided *Only common tests should be described solely by name; describe more complex techniques in the Methods section.*
☐	☒ A description of all covariates tested
☐	☒ A description of any assumptions or corrections, such as tests of normality and adjustment for multiple comparisons
☐	☒ A full description of the statistical parameters including central tendency (e.g. means) or other basic estimates (e.g. regression coefficient) AND variation (e.g. standard deviation) or associated estimates of uncertainty (e.g. confidence intervals)
☐	☒ For null hypothesis testing, the test statistic (e.g. *F*, *t*, *r*) with confidence intervals, effect sizes, degrees of freedom and *P* value noted *Give P values as exact values whenever suitable.*
☒	☐ For Bayesian analysis, information on the choice of priors and Markov chain Monte Carlo settings
☒	☐ For hierarchical and complex designs, identification of the appropriate level for tests and full reporting of outcomes
☒	☐ Estimates of effect sizes (e.g. Cohen's *d*, Pearson's *r*), indicating how they were calculated

Our web collection on statistics for biologists contains articles on many of the points above.

Software and code

Policy information about availability of computer code

Data collection	Mass photometry data acquisition was conducted using AcquireMP software (Refeyn, Ltd, v1.2.3). In vivo imaging of fluorescence signal was performed using a Xenogen IVIS Imaging System 200 and the Living Image software (PerkinElmer, v4.8.0).
Data analysis	For FRET assays, flow cytometry, transwell invasion assays, viability assays and in vivo experiments, data were analyzed and plotted using the software GraphPad Prism 9. For X-ray data processing and analysis: data were processed with XDS and structures were solved by a combination of Se-SAD phasing in Phenix and molecular replacement with PHASER. Refinement was performed with Phenix. Iterative cycles of model building with Coot and restrained refinement were performed. Figures related to X-ray analyses of crystal structures were prepared using PyMOL (The PyMOL Molecular Graphics System, Schrödinger, LLC., v2.5.5). The mass spectrometry spectra were deconvoluted using Protein Deconvolution Software (Thermo Fisher Scientific, Waltham, MA, USA, v4.0). Mass photometry data were processed and analyzed with Discover MP software (Refeyn Ltd, v1.2.3). In vivo imaging data were analyzed with Living Image software (PerkinElmer, v4.8.0). Flow cytometry data was analysed using FlowJo (Becton Dickinson and Co., USA, v10.9.0). Image preparation and analysis for PET/SPECT was done using the PMOD software (PMOD technologies, version 3.709, Zurich, Switzerland).

For manuscripts utilizing custom algorithms or software that are central to the research but not yet described in published literature, software must be made available to editors and reviewers. We strongly encourage code deposition in a community repository (e.g. GitHub). See the Nature Portfolio guidelines for submitting code & software for further information.

Data

Policy information about availability of data

All manuscripts must include a data availability statement. This statement should provide the following information, where applicable:

- Accession codes, unique identifiers, or web links for publicly available datasets
- A description of any restrictions on data availability
- For clinical datasets or third party data, please ensure that the statement adheres to our policy

The atomic models related to this study have been deposited to the Protein Data Bank (PDB, https://www.wwpdb.org/) under accession codes 8PI3 and 8RND. Raw and analysed data associated to Figure 1 and Extended Data Figure 2, as well as NNPI sequences and original gel scans are provided as Source Data files.

Research involving human participants, their data, or biological material

Policy information about studies with human participants or human data. See also policy information about sex, gender (identity/presentation), and sexual orientation and race, ethnicity and racism.

Reporting on sex and gender	N/A
Reporting on race, ethnicity, or other socially relevant groupings	N/A
Population characteristics	N/A
Recruitment	N/A
Ethics oversight	N/A

Note that full information on the approval of the study protocol must also be provided in the manuscript.

Field-specific reporting

Please select the one below that is the best fit for your research. If you are not sure, read the appropriate sections before making your selection.

☒ Life sciences ☐ Behavioural & social sciences ☐ Ecological, evolutionary & environmental sciences

For a reference copy of the document with all sections, see nature.com/documents/nr-reporting-summary-flat.pdf

Life sciences study design

All studies must disclose on these points even when the disclosure is negative.

Sample size	For vavP-Bcl2 mice, the estimated effect size for the difference in the number of B-cells in the spleen of animals is large when comparing wild-type and genetically modified CTSS KO mice, which meant that a sample size of 3 mice per group could be enough to observe a significant difference in case of a full CTSS KO. Even though we were aiming to obtain the same phenotype, the experimental set up was different thus the sample size could not be directly transposed. Since we treated the mice with an inhibitor for a limited time-frame , starting only at 18-30 weeks after birth, we expected a smaller effect size when assessing the difference in tumor development. Since we were working with pharmacological inhibitors that are never 100% effective and can introduce additional variability, we hypothesized based on our experience, that 5 mice per treatment group would be sufficient to detect a significant difference between treatment groups if the inhibitor was effective. For the imaging of CTSS enzymatic activity, we did not find in the literature examples of in vivo comparison of cathepsin activity in wild-type versus cathepsin KO models or upon CTSS inhibitor treatment, so we could not estimate the effect size a priori. Based on similar experiments reported in the literature to study the activity of other cathepsins in vivo using the same molecular probe (Verdoes et al., J Am Chem Soc., 2013), we decided to use 3 mice per treatment group. For the biodistribution experiments, the number of animals was chosen based on what is suggested by the literature and normally used for these standard experiments (see for example Delage et al., Cancers, 2021).
Data exclusions	No data were excluded from the analyses.
Replication	All molecular, biochemical and cellular assays presented in this study were replicated independently twice or more, and the results of all the replicate experiments are described in the article.
Randomization	vavP-Bcl2 mice were randomized in the treatment groups without any knowledge about tumor development. They were allocated randomly to the treatment groups, ensuring that mice of comparable age were assigned to each group. For the imaging of CTSS enzymatic activity in vivo, allocation to treatment groups was not random but based on tumor volume, to have mice with similar tumor volumes in each group. Analogously, for the biodistribution experiments, allocation to treatment groups was not random but based on tumor volume, to have mice

with similar tumor volumes in each group.
No special randomization criterion was needed for our molecular, biochemical and cellular experiments.

Blinding

For the in vivo experiments, during data collection, blinding of the experimenter was not relevant because data was collected in parallel for all animals using the same appropriate instruments and keeping the same acquisition parameters for all samples, therefore data collection could not be biased.

For all the other experiments, data collection was performed for all samples in parallel with automatized instruments (e.g. SpectraMax iD3 plate reader for fluorescence detection), therefore blinding of the experimenter was not required.

Reporting for specific materials, systems and methods

We require information from authors about some types of materials, experimental systems and methods used in many studies. Here, indicate whether each material, system or method listed is relevant to your study. If you are not sure if a list item applies to your research, read the appropriate section before selecting a response.

Materials & experimental systems

n/a	Involved in the study
☐	☒ Antibodies
☐	☒ Eukaryotic cell lines
☒	☐ Palaeontology and archaeology
☐	☒ Animals and other organisms
☒	☐ Clinical data
☒	☐ Dual use research of concern
☒	☐ Plants

Methods

n/a	Involved in the study
☒	☐ ChIP-seq
☐	☒ Flow cytometry
☒	☐ MRI-based neuroimaging

Antibodies

Antibodies used

PE mouse anti-human CD74 (clone Pin.1, Biolegend, cat #357604); BV711 rat anti-mouse CD74 (Clone In-1, BD Biosciences, cat #740748, diluted 1:200); APC-Cy7 rat anti-mouse CD45 (clone 30F11, BD Bioscience, cat #557659); PE-CF594 rat-anti mouse B220 (clone RA3-6B2, BD Bioscience, cat #562313); BV786 hamster anti-mouse CD3 (clone 145-2C11, BD Bioscience, cat #564379); PerCP efluor710 rat anti-mouse CD4 (clone RM4-5, Thermo Fisher Scientific, cat #46-0042-82); PE-Cy7 rat anti-mouse CD8a (clone 53-6.7, BD Bioscience, cat #552877).
Anti-his-Tag primary antibody (Cell Signaling, cat #D3I10); IRDye 800CW goat anti-Rabbit secondary IgG antibody (LICOR, cat #926-32211); goat anti-human Cathepsin S (Bio-Techne, cat #AF1183); rabbit anti-human Cathepsin B XP Rabbit mAb (clone D1C7Y, Cell Signaling, cat #31718), anti-His-Tag XP rabbit mAb (clone D3I1O, Cell Signaling, cat #12698), mouse anti-human alpha-Tubulin (clone B-5-1-2, Sigma Aldrich, cat #T6074); IRDye 680RD goat anti-Mouse IgG (LI-COR, cat #926-68070); goat anti-rabbit antibody (H+L) (Merck Millipore, cat #AP307P), goat anti-mouse antibody (H+L) (Merck Millipore, cat #AP308P), rabbit anti-goat IgG (H+L) (ThermoFisher scientific, cat #31402).

Validation

All the antibodies used in this study were validated for use in the context of the species of interest by the manufacturer. Furthermore, all the primary and secondary antibodies used are standard products already reported multiple times in the literature for the same applications, and we used them only for applications for which they had been validated.

Eukaryotic cell lines

Policy information about cell lines and Sex and Gender in Research

Cell line source(s)

Mouse Diffuse Large B cell Lymphoma cell line A20 were obtained from ATCC (at #ATCC-TIB208, BALB/c background) .
A20-HA-GFP cell line expressing hemagglutinin (HA) gene from influenza virus strain A/Puerto Rico/8/1934 H1N1 (UniProtKB-P03452) were originally provided by Novimmune SA.
HEK293E cells were obtained from Life Technologies (Invitrogen).
ExpiCHO cells were obtained as part of the ExpiCho Expression System from Thermo Fisher Scientific (cat #A29133).
Human Raji, BT-474, Karpas-422, HCC-1569, SU-DHL-4, RT-4 and PC-3 cell lines were obtained from ATCC, whereas human WSU-DLCL2 were obtained from the DSMZ repository.

Authentication

The cell lines used in this study were authenticated by STR DNA profiling.

Mycoplasma contamination

The cell lines used in this study were tested for mycoplasma contamination when they were obtained and all tested negative.

Commonly misidentified lines
(See ICLAC register)

No commonly misidentified cell lines were used in this study.

Animals and other research organisms

Policy information about studies involving animals; ARRIVE guidelines recommended for reporting animal research, and Sex and Gender in Research

Laboratory animals	In vivo experiments involving subcutanous injection of Raji cells were performed on 8-10-week-old NSG mice (NOD.Cg-Prkdcscid Il2rgtm1Wjl/SzJ). For the experiments involving treatment of a transgenic lymphoma mouse model, vavP-Bcl2 mice were used and treatment was started when the mice were 21-30 weeks old. For the T-cell assay: HA-specific TCR CD8+ T cells were isolated from the spleen of CL4 TCR transgenic mice (8-12 weeks old). Mice were kept in a 12 hours-light / 12 hours-dark cycle, at 18-23°C with 40-60% ambient humidity, as recommended and in accordance with the regulations of the Animal Welfare Act (SR 455) and Animal Welfare Ordinance (SR 455.1).
Wild animals	The study did not involve wild animals.
Reporting on sex	In vivo studies were performed on female mice.
Field-collected samples	The study did not involve samples collected from the field.
Ethics oversight	All animal experiments were performed in accordance with the Swiss Federal Veterinary Office guidelines and as authorized by the Cantonal Veterinary Office (animal licenses VD2932.1, VD2993, VD3631 and VD3701).

Note that full information on the approval of the study protocol must also be provided in the manuscript.

Plants

Seed stocks	*Report on the source of all seed stocks or other plant material used. If applicable, state the seed stock centre and catalogue number. If plant specimens were collected from the field, describe the collection location, date and sampling procedures.*
Novel plant genotypes	*Describe the methods by which all novel plant genotypes were produced. This includes those generated by transgenic approaches, gene editing, chemical/radiation-based mutagenesis and hybridization. For transgenic lines, describe the transformation method, the number of independent lines analyzed and the generation upon which experiments were performed. For gene-edited lines, describe the editor used, the endogenous sequence targeted for editing, the targeting guide RNA sequence (if applicable) and how the editor was applied.*
Authentication	*Describe any authentication procedures for each seed stock used or novel genotype generated. Describe any experiments used to assess the effect of a mutation and, where applicable, how potential secondary effects (e.g. second site T-DNA insertions, mosiacism, off-target gene editing) were examined.*

Flow Cytometry

Plots

Confirm that:

☒ The axis labels state the marker and fluorochrome used (e.g. CD4-FITC).

☒ The axis scales are clearly visible. Include numbers along axes only for bottom left plot of group (a 'group' is an analysis of identical markers).

☒ All plots are contour plots with outliers or pseudocolor plots.

☒ A numerical value for number of cells or percentage (with statistics) is provided.

Methodology

Sample preparation	For the T-cell assay: HA-specific TCR CD8+ T cells were isolated from the spleen of CL4 TCR transgenic mice. The spleen was smashed, the cells were washed in PBS, resuspended in RBC lysis buffer (Miltenyi Biotec, cat #130-094-183) for 4 minutes at room temperature to lyse red blood cells, PBS was added to stop lysis and cells were filtered through a 40 µm filter (Falcon, #352350) to generate a single cell suspension. Single cell suspension was then processed through a negative mouse CD8 T cell (Miltenyi Biotec, cat #130-104-075) isolation kit following the manufacturer's instructions. A20-HA lymphoma cells WT, Ctss KO, or B2m KO, expressing HA (hemagglutinin) as antigen were pre-treated with the indicated compounds for 16 hours and then co-incubated for 72 h with CellTrace Violet-stained (Thermo Fisher, cat #C34557) CD8+ T cells isolated from CL4-HA transgenic animals, in presence or absence of treatment. At the end of the lymphoma cells/T cells co-culture, cells were collected, stained with DAPI viability dye (Thermo Fisher, cat #D1306) and analyzed for the proliferation of T cells by quantifying CellTrace Violet proliferation peaks, using a LSR Fortessa flow cytometer (BD Biosciences). The absolute number of A20 lymphoma cells in each sample was also assessed through the use of CountBright Absolute Counting Beads (Thermo Fisher, cat #C36950), by comparing the ratio of bead events to cell events for each sample. For flow cytometry analysis of spleens harvested from in vivo experiments: the spleens were smashed, the cells were washed in PBS, resuspended in RBC lysis buffer (Miltenyi Biotec, cat #130-094-183) for 4 minutes at room temperature to lyse red blood cells, PBS was added to stop lysis and cells were filtered through a 40 µm filter (Falcon, #352350) to generate a single cell suspension. After cell counting, 2x10e6 cells were incubated with 50 µl of Fc Block (BD Biosciences, cat #553142) 1:50 solution in FACS buffer [PBS (Gibco/Thermofisher scientific, cat #10010-015), 2% BSA (Sigma Aldrich, cat #A7906] for 15 min

	on ice. Samples were subsequently supplemented with 50 µl of the following antibody mixture: APC-Cy7 rat anti-mouse CD45 (clone 30F11, BD Bioscience, cat #557659), PE-CF594 rat-anti mouse B220 (clone RA3-6B2, BD Bioscience, cat #562313), BV786 hamster anti-mouse CD3 (clone 145-2C11, BD Bioscience, cat #564379), PerCP efluor710 rat anti-mouse CD4 (clone RM4-5, Thermo Fisher Scientific, cat #46-0042-82), PE-Cy7 rat anti-mouse CD8a (clone 53-6.7, BD Bioscience, cat #552877). Samples were then washed three times, resuspended in 200 µl of FACS buffer containing DAPI viability marker (Molecular probes, cat #D1306), and analyzed using LSR Fortessa flow cytometer (BD Biosciences).
Instrument	LSR Fortessa flow cytometer (BD Biosciences)
Software	Flow cytometric analyses were performed with FlowJo V10.9.0 software (Tree Star, Ashland, OR USA).
Cell population abundance	Cell sorting was not performed in this study.
Gating strategy	The complete gating strategy is exemplified in the Supplementary Information. In brief, single cells were gated using FSC-H/FSC-A and SSC-H/SSC-A gating; then, live cells were gated using DAPI-negative gating; among live cells, leukocytes were then gated using CD45+ gating; among leukocytes, CD3/B220 gating allowed to separate T cells (CD3+) from B cells (B220+); finally, among CD3+ T cells, CD4/CD8 gating was used to identify CD4 T cells and CD8 T cells (as CD4+ and CD8+ cells respectively).

☒ Tick this box to confirm that a figure exemplifying the gating strategy is provided in the Supplementary Information.